Geometric confinement controls stiffness, strength, extensibility and toughness in poly(urethane-urea) copolymers

Oguzhan Oguz[1,2,*], Nicolas Candau[3], Gregory Stoclet[4], Eren Simsek[1,†], Cagla Kosak Soz[5], Emel Yilgor[5], Iskender Yilgor[5,*] and Yusuf Z. Menceloglu[1,2,*]

[1]*Faculty of Engineering and Natural Sciences, Materials Science and Nano Engineering, Sabanci University, 34956, Orhanli, Tuzla, Istanbul, Turkey*

[2]*Sabanci University Integrated Manufacturing Technologies Research and Application Center & Composite Technologies Center of Excellence, Teknopark Istanbul, 34906, Pendik, Istanbul, Turkey*

[3]*Centre Català del Plàstic (CCP) - Universitat Politècnica de Catalunya Barcelona Tech (EEBE-UPC), Av. D'Eduard Maristany, 16, 08019, Spain*

[4]*Unité Matériaux Et Transformations (UMET), UMR CNRS 8207, Université de Lille Nord de France, USTL-ENSCL, Bat C7, BP 90108, 59652 Villeneuve d'Ascq, France*

[5]*KUYTAM Surface Science and Technology Center, Chemistry Department, Koc University, 34450, Sariyer, Istanbul, Turkey*

[†]*Current address: Quantag Nanotechnologies, Barbaros, 34746, Istanbul, Turkey*

[*]*Corresponding authors: oguzhanoguz@sabanciuniv.edu (O. Oguz); iyilgor@ku.edu.tr (I. Yilgor) yusufm@sabanciuniv.edu (Y. Z. Menceloglu)*

ABSTRACT

Achieving a unique combination of stiffness, strength, extensibility and toughness in sol-cast poly(urethane-urea) (PU) copolymer films is a challenge since these properties are -in general- mutually exclusive. Here we demonstrate that geometric confinement of the basic building blocks controls stiffness, strength, extensibility and toughness in PU films. Our results suggest that the severity of geometric confinement can be tuned by adjusting (*i*) soft segment molecular weight (SSMW) and (*ii*) drying temperature (DT) thanks to their effects on the structure formation via micro-phase separation and/or (confined and/or bulk) crystallization. It is therefore possible to produce (*i*) soft (no notable confinement) and (*ii*) stiff, strong, extensible and tough (severe confinement) materials without changing any other parameter except SSMW and DT. The former has a typical physically cross-linked network and shows a well-defined elastomeric behavior with elastic modulus (E) of 5–20 MPa, tensile strength (σ_{max}) of 30–35 MPa, extensibility (ε) of 1000–1300% and toughness (W) of 90–180 MJm^{-3}. The latter, on the other hand, possesses an elegant hierarchical structure containing tightly packed secondary structures (7_2-helix, 4_1-helix and antiparallel β-sheets) and displays an elasto-plastic behavior with E of 400–700 MPa, σ_{max} of 45–55 MPa, ε of 650–850% and W of 200–250 MJm^{-3}. Hence, our findings may be of interest in designing advanced materials containing synthetic replica of the secondary structures found in protein based materials. The structure formation in the materials with this structural hierarchy is driven by the confined crystallization of helical poly(ethylene oxide) (PEO) chains in subnanometer urea channels, which –to the best of our knowledge– is a new phenomenon has not yet reported in PU literature, and complemented by the "bulk" crystallization of PEO and/or the micro-phase separation.

1. INTRODUCTION

Urethane-urea chemistry offers diverse possibilities for design and synthesis of thermoplastic polyurethanes[1-4] (TPUs), i.e., segmented polyurethane, polyurea, and poly(urethane–urea) copolymers, with functional surface and bulk properties. TPUs are, in general, linear macromolecules typically formed by alternating soft and hard segments. Soft segments (SS) are oligomeric diols or diamines with a glass transition temperature (T_g) well below room temperature, catering elastomeric characteristics of TPUs at service temperatures. Hard segments (HS), on the other hand, are obtained by the reaction of diisocyanates with diol or diamine chain extenders and form hydrogen bonded domains having a T_g and/or melting temperature (T_m) well beyond the service window, which act as physical crosslinks providing TPUs with thermoplastic properties.[4-7]

There is plenty of room for designing multi-functional TPUs with tunable morphologies as the number of commercially available basic building blocks with different features is practically unlimited. However, this also indicates a vast number of parameters[4,8] required to be controlled whilst synthesis and processing as they significantly affect both micro-phase separation and crystallization that are the two key -interrelated- phenomena determining structure-property behavior of resulting materials.

These parameters can be roughly divided into two categories as (*i*) *synthesis* and (*ii*) *processing* parameters. *Synthesis parameters* have been comprehensively examined in decades of research,[9-13] whereas *processing parameters* have not yet received as much attention. This is particularly true for solution casting since the relevant studies available in the literature mainly rely on melt-processing.[14-22] Although parameters like (*i*) solvent type, (*ii*) drying atmosphere, (*iii*) drying temperature, (*iv*) residence time at the drying temperature and (*v*) post thermal/cryo- treatments (annealing, quenching etc.) are extremely important to obtain high-quality sol-cast films/sheets, they have been somewhat overlooked in the literature. For instance, most of the sol-cast TPU films/sheets found in the literature have reported to be dried at 60 °C, even though the solvent systems used, and hence their evaporation rates at this temperature, are completely different than each other.[23-25]

To address this issue, here we focus on the effect of drying temperature on the structure-property behavior of a series of poly(ethylene oxide)[26,27] (PEO) based poly(urethane-urea) copolymers with a hard segment content of 30 wt%. PEO oligomers with 2000, 4600 and 8000 g.mol^{-1} molar masses were used as soft segments. Whilst all the other parameters were kept constant, two different drying temperatures (60 °C and 100 °C) were applied to prepare the film specimens that were then comprehensively characterized by a series of techniques.

This has enabled us to demonstrate that geometric confinement of the basic building blocks along the multiple length scales controls stiffness, strength, extensibility and toughness in sol-cast PU films. Our findings suggest that the severity of geometric confinement in sol-cast PU films can be tuned by controlling soft segment molecular weight and drying temperature since these two parameters are of great importance for the structure formation through micro-phase separation and/or (confined and/or bulk) crystallization. This, in return, can be utilized to create entirely different morphologies and hence achieve significant variations in mechanical properties without changing any other parameter. To demonstrate, sol-cast PU films w/o severe geometric confinement are prepared and comprehensively investigated. The films with severe confinement possess a structural hierarchy spanning length scales from angstroms to micrometers, leading to unique combinations of stiffness, strength, extensibility and toughness. Our findings may also be of interest in mimicking certain protein structures containing tightly packed natural design motifs like helices and anti-parallel β–sheets as the structural hierarchy demonstrated here consists of these secondary structures. The structure formation in these films is governed by the confined crystallization of helical poly(ethylene oxide) (PEO) chains in subnanometer urea channels and complemented by the "bulk" crystallization of PEO and the micro-phase separation. The confined crystallization of PEO in subnanometer urea channels is indeed known to create host–guest (inclusion) complexes. However, to the best of our knowledge, it has not yet been demonstrated in PU copolymers. We therefore also show how the α form of these complex crystals is formed and what kind of impacts it has on the structure-property relations of the PU films.

2. EXPERIMENTAL SECTION

2.1. Materials

PEO oligomers with number average molar masses, M_n of 2000, 4600 and 8000 g.mol^{-1} were obtained from Merck. Bis(4-isocyanatocyclohexyl)methane (HMDI) with a purity of >99.5% was kindly provided by Bayer. 2-Methyl-1,5-diaminopentane (MDAP) chain extender was kindly supplied by DuPont. Dibutyltin dilaurate (DBTDL) catalyst was purchased from Witco. Reagent grade tetrahydrofuran (THF) and dimethylformamide (DMF) were also obtained from Merck. All chemicals were used as received.

2.2. Synthesis

The hard segment model compounds (HMDI-MDAP) with molecular weights similar to those of the HSs in the copolymers were prepared as control samples and characterized as given in Figure S1 and S2.

The copolymers were synthesized by the two-step polymerization technique, also known as the prepolymer method. The detailed procedure followed was previously reported by our group.[28-32] All reactions were performed in 500 mL three-necked round-bottom Pyrex reaction flasks equipped with a mechanical overhead stirrer, a thermometer and a funnel, with

temperature control provided by a heating mantle. The isocyanate terminated PEO prepolymer solution in THF with 50 wt% solids content was prepared at 60 °C. 150 ppm of DBTDL catalyst (diluted to 1 wt% in THF solution) was added into the mixture of PEO and HMDI that was stirred for 1 hour at the same temperature. Prepolymer formation was monitored by Fourier transform infrared (FTIR) spectroscopy. The reaction was complete after about 1h. The heat was then turned off and the prepolymer dissolved in DMF to obtain a solution with 25 wt% solids content. Chain extension was carried out at room temperature by dropwise addition of MDAP dissolved in DMF (≈10 wt% solids content) to the prepolymer solution. Completion of the chain extension was also monitored by FTIR spectroscopy. The dropwise addition of MDAP was ceased when the strong isocyanate peak centered on 2260 cm^{-1} completely disappeared. The viscosity increase during the chain extension reaction was controlled by adding DMF into the reaction flask. The chemical structure of the PU copolymers is shown in Figure S3.

2.3. Preparation of PU films for testing

PU films were cast from polymer solution (THF:DMF/1:6.25) into Teflon molds. Two different drying protocols were followed. In the first protocol, the molds were kept at room temperature for 24h in fume hood and then placed in an oven at 60 °C for 24h under vacuum to ensure complete evaporation of the solvent. Samples were then cooled down to room temperature and stored in sealed polyethylene bags minimum 24h before testing. In the second protocol, the same steps were followed but this time the oven was set to 100 °C instead of 60 °C. A list of the PU copolymers investigated, their compositions and drying conditions is provided in Table 1. In the sample nomenclature (PU-X-T), (X) indicated the molecular weight of the PEO used in kilo daltons and (T) the drying temperature in degree of Celsius.

Table 1. Sample notation, compositional details and annealing temperature of the PUs used in this study.

Coding	PEO $<M_n>$ g/mol	PEO Chain Length* (nm)	HS $<M_n>$ g/mol	HS Content (wt %)	Drying Temperature (˚C)
PU-2-60	2000	12.0	860	30	60
PU-5-60	4600	27.3	1970	30	60
PU-8-60	8000	51.2	3400	30	60
PU-2-100	2000	12.0	860	30	100
PU-5-100	4600	27.3	1970	30	100
PU-8-100	8000	51.2	3400	30	100

*PEO segment lengths were taken from the literature.[33]

2.4. Characterization Techniques

Gel Permeation Chromatography (GPC) analyses were performed using a Viscotek GPCmax VE-2001 instrument equipped with D5000-D 3000-D 1000-D Guard columns and RI, LS, DP detectors. DMF was used as the solvent and analysis was performed at 55 °C with a flow rate of 1 mL/min. Polymer solutions were prepared in DMF at a concentration

of 2 mg/mL. The samples were filtered using VMR PTFE syringe filters with average pore size of 0.45 μm before measurements. Average molecular weights were determined using calibration curves obtained from polystyrene standards. Average molecular weights and molecular weight distributions of the copolymers along with the effect of thermal treatment on the samples are listed in Table 2.

Table 2. Average molecular weight and molecular weight distributions of the PEO based polyurethaneureas along with the effect of thermal treatment on the samples.

Notation	$<M_w>$ g/mol	$<M_n>$ g/mol	M_w/M_n
PU-2	100,000	68,000	1.48
PU-2 24 h at 100 °C	106,000	70,400	1.51
PU-5	232,000	164,000	1.42
PU-5 24 h at 100 °C	243,300	168,700	1.44
PU-8	309,000	209,500	1.47
PU-8 24 h at 100 °C	317,000	212,800	1.49

Thermogravimetric analyses were carried out using STA 449C simultaneous thermal analyzer (Netzsch, Germany) under nitrogen atmosphere with a heating rate of 3 °C/min, from ambient temperature to 700 °C.

Modulated Differential Scanning Calorimetry (MDSC) analyses were performed by a TA Q2000 instrument calibrated with indium standard and equipped with Tzero functionality that significantly improves the baseline via compensating resistance and capacitance imbalances. In this technique, a harmonic modulation is applied on a typical DSC linear ramp. Then the typical DSC thermograms are deconvoluted by a signal analysis process into two different components mainly referred as reversing and non-reversing ones. The reversing component involves the reversible events in the time scale of modulation such as the glass transition step and melting of outer layers of crystallites. Apart from this, melting of crystal cores and enthalpy relaxation accompanying the glass transition are mainly characterized by the non-reversing component.[33-35]

All measurements were performed in the range of -160 and 250 °C at a rate 3 °C/min and a modulation ±1 °C over a period of 90 s. We applied a typical procedure for the sample preparation. For each composition, a small piece of thin film sample, weighting around 10 mg, was encapsulated in a hermetic DSC pan prior to measurement. At least five specimens were measured for each sample. Overall thermal properties of the samples were followed by the total specific heat flow signals as a function of temperature. As the copolymers with PEO-4600 and PEO-8000 soft segments display very weak glassy-rubbery transitions, it is not easy to detect the soft segment glass transition temperature. For this reason, the reversing signal is used to analyze the glassy-rubbery transition region for all the samples under investigation. Glass transition temperature (T_g) and the heat capacity change at T_g (ΔC_p *at* T_g) were determined by the inflection point and the tangent

methods, respectively. The degree of soft segment crystallinity (χ_c) is calculated using the equation given below, assuming that the hard segment does not contribute to the crystallinity of the soft segment:

$$\chi_c = \frac{\Delta H_m - \Delta H_c}{(1 - X_{HS}) \times \Delta H_{100\%,PEO}} \times 100\%$$

where ΔH_m and ΔH_c the enthalpy changes obtained from the areas of the respective endothermic and exothermic peaks, X_{HS} is the weight fraction of the hard segment. The melting enthalpy for the 100% crystalline polymer is considered to be equal to that of pure PEO ($\Delta H_{100\%PEO}$), which is denoted as 196.6 J/g.[33, 35]

X-ray Diffraction (XRD) measurements of the film samples were performed on a Bruker D8 Advance X-ray Diffractometer using Ni-filtered Cu-Kα radiation (λ=0.1542 nm). All the measurements were performed from 5 up to 90° with a step size of 0.01°. The results were plotted as a function of the scattering angle 2θ. During the measurements, specific instrumental and sample effects were also considered. The d-spacing is calculated with respect to Bragg law, nλ = 2dsinθ, where λ is the wavelength of the radiation, d is the inter-planar spacing, θ is the diffraction angle, and n is the order of the reflection. At least five specimens of each sample were measured and then analyzed for determining the total degree of crystallinity values presented in the respective section.

Fourier Transform Infrared Spectroscopy (FTIR) measurements were performed on a Nicolet 7600 Spectrometer. For the progress and completion of the synthesis, solutions were cast on KBr discs and thin films were obtained after evaporating the solvent with an air gun. 32 scans were taken for each spectrum with a resolution of 2 cm^{-1}. A Thermo Scientific Nicolet iS10 Spectrometer equipped with a Thermo Scientific Smart iTR™ Accessory with Diamond ATR crystal and with an incident angle of 42° was used to record ATR-IR (Attenuated Total Reflectance Infrared Spectroscopy) spectra of the film samples prepared under different thermal protocols. 32 scans were taken for each spectrum with a resolution of 2 cm^{-1} in the range of 4000–400 cm^{-1}. All spectral corrections, such as background substraction, were carefully performed by Omnic Software. Deconvolution of the amide-I and amide-II bands was performed using Origin® data processing software. A linear baseline was used. The peak maxima were denoted as the frequencies detected by second derivative analysis. Lorentzian peak function was applied throughout the non-linear fitting process. Quantification of the secondary structures was performed by analyzing the amide-I region. The average percent fractions of the secondary structures were calculated by integrating the area under each deconvoluted peak, and then normalizing to the total area of the amide-I region. At least five specimens of each material were measured by ATR-IR technique, and then analyzed by the deconvolution procedure summarized above to determine the standart deviations for the respective quantities.

Renishaw Invia Raman spectrometer (equipped with 785, 633, 532 nm excitation laser sources) was used to obtain the Raman spectra of the samples at the excitation wavelength of 633 nm. To avoid the structural deterioration, 50% laser

power was used to excite the sol-cast films with an average thickness of 0.2 mm. Each measurement accumulates the signal for 1 min with an exposure time of 10 sec under ambient temperature and humidity conditions.

A Nikon Eclipse ME 600 optical microscope (OM) equipped with a hot stage was used to investigate the micron scale morphologies of thin polymer films placed between two clean glass slides. All measurements were performed under the polarized light in bright field.

Atomic Force Microscopy (AFM) images of the free surface of completely dried solution cast films were captured on a Bruker ScanAsyst enabled Multimode-8 Atomic Force Microscope equipped with a Nanoscope 8.1 controller. All samples were analyzed in standard tapping/non-contact mode by using a Bruker Scanasyst Air probe with a nominal spring constant of 0.4 N/m, resonance frequency of 70 kHz and a radius of curvature of 2 nm. All images were recorded at 1 Hz frequency with 512x512 scan and a set point ratio of ~ 0.6 at ambient temperature and humidity conditions.

Stress-strain analyses were performed on dog-bone type specimens punched out of thin films using a standard die (ASTM D 1708). Measurements were made on a Zwick Z100 model tester under ambient temperature and humidity conditions with a crosshead speed of 25.0 mm/min (L_o= 24.0 mm). At least five specimens were tested for each sample.

3. RESULTS AND DISCUSSION

3.1. Thermal Stability

TGA and GPC measurements were performed to check the effect of drying protocols on the specimens. For the thermal stability measurements, the samples were subjected to the same experimental conditions applied in DSC analyses, i.e. at a heating rate of 3 °C/min under nitrogen atmosphere, during TGA analyses. Figure S4 displays the weight loss as a function of temperature for the samples. The decomposition starts around 330 °C, which is well above the temperatures applied in our drying protocols, for PU-2, PU-5 and PU-8, respectively. However, side reactions like chain scission and possible recombination (e.g., by cleavage of urethane and/or urea bonds) are not followed by TGA measurements. In general, such reactions give rise to change in the molecular weight and/or molecular weight distribution of the materials.[36] As listed in Table 2, GPC results suggest that no notable change is occurred in the molecular weights and molecular weight distributions of the samples after drying at 100 °C. These results suggest that there is no substantial degradation taking place in our copolymers .

3.2. Calorimetry

Modulated DSC analyses were performed to investigate the thermal properties of the samples, which were evaluated using the data obtained from the first heating scans of the specimens since the mechanical properties can only be influenced by the thermal histories of the materials rely on the applied processing conditions. The total heat flow signals of the PU copolymers are provided in Figure 1.

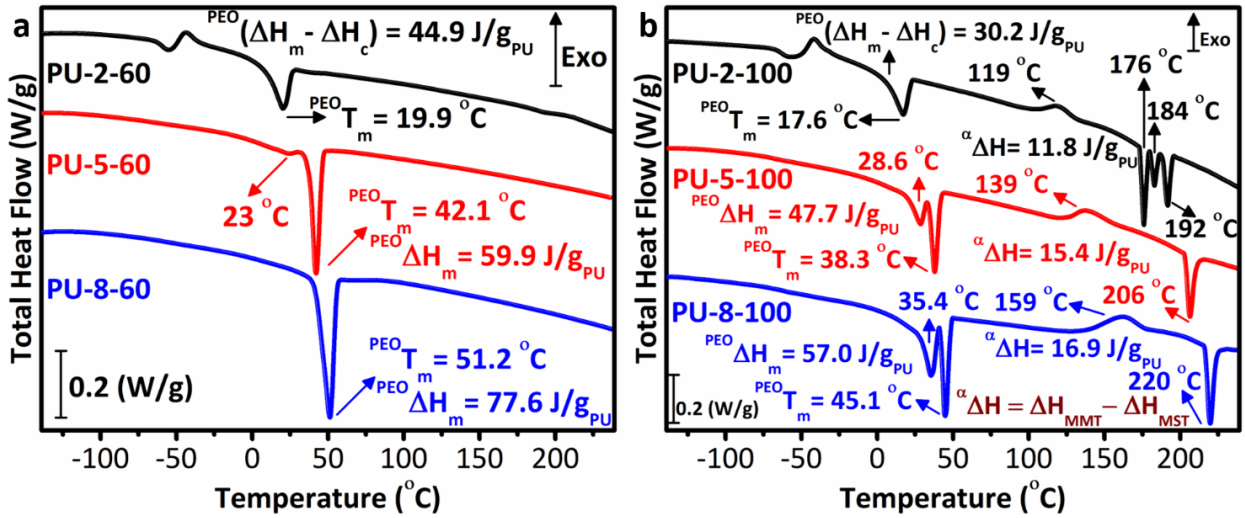

Figure 1. Total heat flow signals as a function of temperature obtained from MDSC analyses of the samples dried at (a) 60 °C and (b) 100 °C.

In Figure 1a, PU-2-60 shows a well-defined glassy-rubbery transition between -60 and -50 °C followed by a small exotherm between -50 and -25 °C and an endotherm at 19.9 °C with a ${}^{PEO}(\Delta H_m - \Delta H_c)$ of 44.9±4.3 J/g$_{PU}$. PU-5-60 and PU-8-60 display very weak glassy-rubbery transitions at temperatures between -60 and -40 °C followed by sharp endotherms at 42.1 and 51.2 °C with enthalpy changes of 59.9±5.2 J/g$_{PU}$ and 77.6±3.7 J/g$_{PU}$, respectively. No other high temperature exothermic and/or endothermic transitions are observed for the samples prepared at 60 °C.

In Figure 1b, PU-2-100 displays a distinct glass transition followed by an exotherm between -50 and -25 °C and an endotherm at 17.1 °C with a ${}^{PEO}(\Delta H_m - \Delta H_c)$ of 30.2±3.1 J/g$_{PU}$. PU-2-100 also shows another exotherm with a peak temperature of 119 ˚C and multiple endotherms with peak temperatures of 176, 184 and 192 °C in the high temperature region. PU-5-100 and PU-8-100 show weak glass transition steps at temperatures between -70 °C and -60 °C, followed by bimodal endotherms in the intermediate regions of the thermograms. The bimodal endotherm of PU-5-100 comprises a relatively small endotherm apparent as a shoulder with a peak temperature of 28.6 °C and a main endotherm with a peak temperature of 38.3 °C and a total enthalpy change (shoulder and main peak) of 47.7±3.4 J/g$_{PU}$, whereas a shoulder with a peak temperature of 35.4 °C and a main endotherm with a peak temperature of 45.1 °C and a total enthalpy change of 57.0±3.0 J/g$_{PU}$ are observed in that of PU-8-100. In addition, PU-5-100 displays an exotherm with a peak temperature of 139 °C followed by an endotherm with a peak temperature of 206 °C in the high temperature region of the thermogram. Similarly, PU-8-100 shows an exotherm with a peak temperature of 159 °C and an endotherm with a peak temperature of 220 °C. These results are elaborately discussed in (*i*) *soft segment glass transition,* (*ii*) *melting of PEO soft segment crystals and soft segment crystallinity,* and *(iii) micro-phase separation/mixing* subsections in the following. The ${}^{\alpha}\Delta H$ values given in Figure 1b and respective discussion are provided in the *micro-phase separation/mixing* subsection. In addition, the

enthalpy changes given in Figure 1 ($^{PEO}\Delta H_m$, $^{PEO}(\Delta H_m - \Delta H_c)$) are not the ones normalized by the weight fraction of PEO. The normalized values used to calculate soft segment crystallinity values are denoted in the *melting of PEO soft segment crystals and soft segment crystallinity* subsection. It should also be noted that the soft segment glass transition temperatures were determined using the reversing heat flow signals in Figure 2 and 3 as discussed in the *soft segment glass transition* subsection in the following.

***Soft segment glass transition*:** The transition located at between -70 °C and -40 °C is assigned to the soft segment (PEO) glass transition ($^{PEO}T_g$), which is mainly followed by the reversing heat flow signals using the inflection point method. To provide a clear overview on the effects of soft segment molecular weight and drying protocol, the reversing heat flow signals for the corresponding temperature range is replotted in Figure 2 and 3 for all the samples investigated.

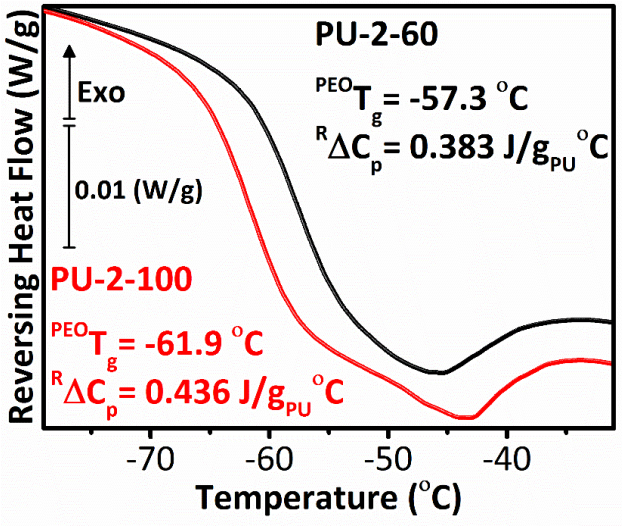

Figure 2. Reversing heat flow thermograms of the copolymers based on PEO-2000 soft segment (PU-2-60 and PU-2-100) at temperatures between -80 °C and -30 °C. The uncertainties in $^{PEO}T_g$ and $^{R}\Delta C_p$ *at* $^{PEO}T_g$ values on the plot are ±1 °C and ±0.02 J/g°C, respectively.

$^{PEO}T_g$ values are determined as -57.3 °C and -61.9 °C for PU-2-60 and PU-2-100, respectively (Figure 2). The corresponding $^{R}\Delta C_p$ *at* $^{PEO}T_g$ values are calculated as 0.383 J/g°C (PU-2-60) and 0.436 J/g°C (PU-2-100). $^{PEO}T_g$ values of PU-5-60 and PU-5-100 copolymers are determined as -53.8 °C and -63.6 °C, respectively (Figure 3a). The corresponding $^{R}\Delta C_p$ *at* $^{PEO}T_g$ values are calculated as 0.072 J/g°C (PU-5-60) and 0.123 J/g°C (PU-5-100). $^{PEO}T_g$ values of PU-8-60 and PU-8-100 are recorded as -49.3 °C and -68.7 °C, respectively (Figure 3b). The respective $^{R}\Delta C_p$ *at* $^{PEO}T_g$ values are denoted as 0.043 J/g°C (PU-8-60) and 0.162 J/g°C (PU-8-100).

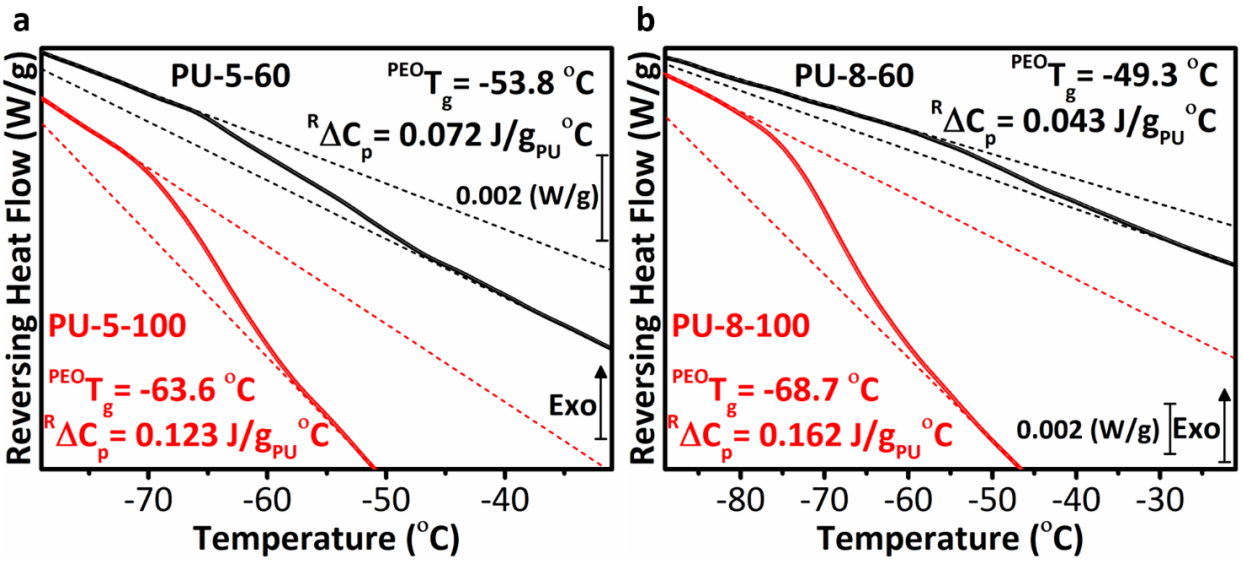

Figure 3. Reversing heat flow thermograms of the copolymers based on (a) PEO-4600 (PU-5-60 and PU-5-100) and (b) PEO-8000 soft segments (PU-8-60 and PU-8-100). The uncertainties in ${}^{PEO}T_g$ and ${}^{R}\Delta C_p$ *at* ${}^{PEO}T_g$ values on the plot are ±1 °C and ±0.02 J/g°C, respectively.

The ${}^{PEO}T_g$ values are plotted in Figure 4 as a function of soft segment molecular weight for both series of the samples. The ${}^{PEO}T_g$ increases with increasing SSMW for PU-X-60 set of the samples. The increasing trend in ${}^{PEO}T_g$ values with increasing SSMW is basically arisen from two different reasons. One of them is the increasing amount of dissolved hard segments in the soft matrix, and the other one is the increasing amount of PEO soft segment crystals formed by bulk crystallization of the soft segments. In contrast, the ${}^{PEO}T_g$ decreases via increasing SSMW for PU-X-100 set of the samples. For all the PU copolymers investigated (PU-2, PU-5 and PU-8), the decrease in ${}^{PEO}T_g$ is induced by drying at 100 °C.

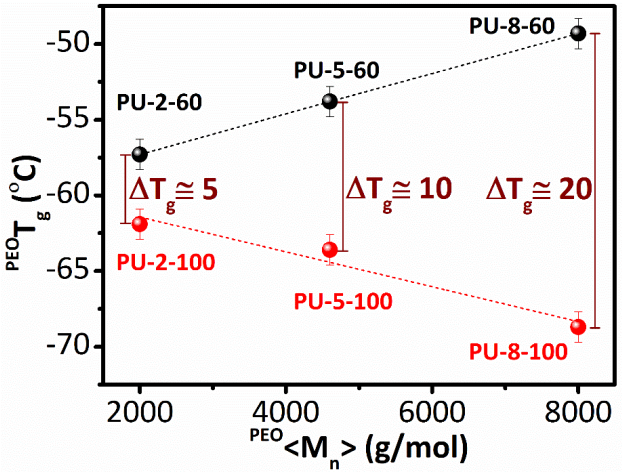

Figure 4. The change in the soft segment (PEO) glass transition as a function of SSMW for both series of the samples dried at 60 °C and 100 °C. ${}^{PEO}T_g$ increases with increasing SSMW for the samples dried at 60 °C. In contrast, this trend becomes reverse, i.e., ${}^{PEO}T_g$ decreases with increasing SSMW, for the ones dried at 100 °C. ΔT_g is calculated as the absolute value of ${}^{PU\text{-}X}\Delta T_g = {}^{PU\text{-}X\text{-}60}T_g - {}^{PU\text{-}X\text{-}100}T_g$, where X indicates the molecular weight of the PEO used in kilo daltons for the copolymers based on PEO-2000, PEO-4600 and PEO-8000 soft segments.

This leads to an increase in the miscibility between the hard and soft segments, i.e. more hard and soft segments participate in a "phase mixing" process. At this stage, PEO and urea molecules act cooperatively to minimize their free energies. This initiates confined crystallization of the PEO chains within the subnanometer urea channels giving rise to the formation of PEO-Urea α-complex crystals. Structural details for this complex crystal is provided in the following sections via XRD, FT-IR, Raman and microscopic analyses. Formation of the α-complex crystals simultaneously activates separation of the molecules participating in this phase from the bulk. As the SSMW increases, the hard segment molecular weight increases too, and thus, the number of both PEO and urea molecules participating in this process also increases. This corresponds to the same amount of decrease in the number of dissolved hard segments creating physical constraints on the mobility of the PEO chains in the bulk. This means the removal of same amount of constraints on the mobility, which results in an enhanced mobility as characterized by the decrease in ${}^{PEO}T_g$. For this reason, increasing SSMW results in a decreasing trend in ${}^{PEO}T_g$ for PU-X-100 set of the samples.

Figure 4 also shows the change in ${}^{PEO}T_g$ values (ΔT_g) originated from the thermal annealing. ΔT_g defined in this study is different than the one usually described in TPUs to investigate the degree of micro-phase separation. In conventional TPUs, ΔT_g is defined as the absolute value of the difference between T_g of the soft segment in TPUs, (${}^{SS}T_g$), and of the pure oligomers/macrodiols, (${}^{oligomer}T_g$) used as the soft segment during the synthesis that can be quantified as $\Delta T_g = {}^{SS}T_g - {}^{oligomer}T_g$. In this respect, it is assumed that higher value of ΔT_g indicates higher miscibility, and thus, an increasing trend in ΔT_g implies an increasing miscibility due to favorable interactions between the hard and soft segments.[37] In return, it is assumed that a lower value of ΔT_g suggests a higher degree of phase separation. However, Saiani *et. al.* have reported that the determination of the phase separation degree from the soft segment phase glass transition does not seem to be adequate for high hard block content TPUs displaying high temperature endothermic peaks like micro-phase mixing temperature (T_{MMT}).[36]

They have also denoted that even for such samples, some degree of micro-phase separation is present even if ${}^{SS}T_g$ is not observed.[36] On this basis, it should be emphasized that here we define ΔT_g as the absolute value of ${}^{PU\text{-}X}\Delta T_g = {}^{PU\text{-}X\text{-}60}T_g - {}^{PU\text{-}X\text{-}100}T_g$, where X indicates the molecular weight of the PEO used in kilo daltons, to only demonstrate the increasing miscibility in the samples prepared at 100 °C compared to the ones prepared at 60 °C. As shown in Figure 4, ΔT_g systematically increases with increasing soft segment molecular weight. However, this does not necessarily mean that an increasing trend in SSMW implies a decreasing trend in the degree of micro-phase separation due to the fact that formation of the α-complex crystals suggests that these two processes, i.e., a phase mixing and a phase separation, can simultaneously work in a cooperative manner since the urea molecules are highly organized by bidentate hydrogen bonds between each other on the walls of the channels while confined PEO chains are tightly hydrogen bonded to the excess urea molecules

within the channels during the structure formation. The process on the walls of the channels represents the phase separation, whereas the one within the channels illustrates the phase mixing in terms of the type and extent of intermolecular interactions, i.e., hydrogen bonds, which is generally used to describe these two processes in the literature.

***Melting behavior of PEO soft segment crystals and soft segment crystallinity*:** As shown in Figure 1, the endothermic peaks at 19.9, 42.1 and 51.2 °C are attributed to the melting points ($^{PEO}T_m$) of PEO soft segment crystals in PU-2-60, PU-5-60 and PU-8-60, respectively. After the normalization of the enthalpy changes provided in Figure 1a with the weight fraction of PEO, $(\Delta H_m - \Delta H_c)$ of 64.1±6.1, ΔH_m of 85.5±7.4, and ΔH_m of 110.9±5.3 J/g_{PEO} are obtained for PU-2-60, PU-5-60 and PU-8-60, respectively. Using the normalized enthalpy changes, the degree of soft segment crystallinity ($^{PEO}\chi_c$) values of the samples are calculated as $^{PEO}\chi_{c\text{-}PU\text{-}2\text{-}60}$ (%) = 32.6±3.1, $^{PEO}\chi_{c\text{-}PU\text{-}5\text{-}60}$ (%) = 43.5±3.8, and $^{PEO}\chi_{c\text{-}PU\text{-}8\text{-}60}$ (%) = 56.4±2.7 for PU-2-60, PU-5-60 and PU-8-60, respectively. $^{PEO}T_m$ and $^{PEO}\chi_c$ values increase with increasing molecular weight.

For the samples prepared at 100 °C, $^{PEO}T_m$ of PEO values are recorded as 17.6, 38.3 and 45.1 °C for PU-2-100, PU-5-100 and PU-8-100, respectively. The corresponding $^{PEO}\chi_c$ values of this set of samples are calculated as $^{PEO}\chi_{c\text{-}PU\text{-}2\text{-}100}$ (%) = 21.9±2.3, $^{PEO}\chi_{c\text{-}PU\text{-}5\text{-}100}$ (%) = 34.6±2.5, and $^{PEO}\chi_{c\text{-}PU\text{-}8\text{-}100}$ (%) = 41.4±2.2 after the normalization of the respective enthalpy changes given in Figure 1b with the weight fraction of PEO, which correspond to $(\Delta H_m - \Delta H_c)$ of 43.1±4.5, ΔH_m of 68.1±4.9, and ΔH_m of 81.4±4.3 J/g_{PEO} for PU-2-100, PU-5-100 and PU-8-100, respectively.

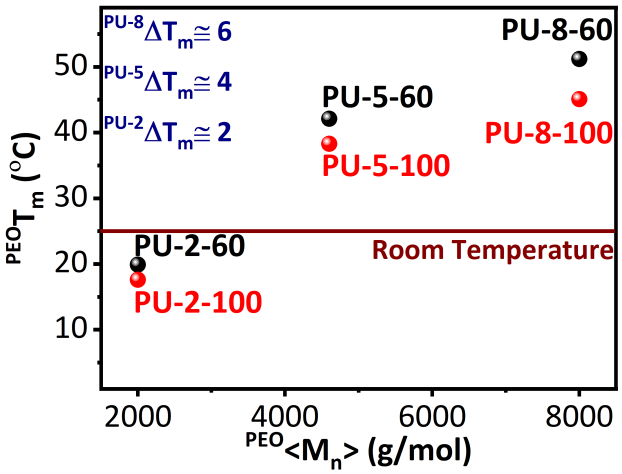

Figure 5. The change in the melting point of PEO soft segment crystals ($^{PEO}T_m$) as a function of SSMW and drying temperature: Effect of SSMW; $^{PEO}T_{m(PU\text{-}8\text{-}60)} > {}^{PEO}T_{m(PU\text{-}5\text{-}60)} > {}^{PEO}T_{m(PU\text{-}2\text{-}60)}$, and $^{PEO}T_{m(PU\text{-}8\text{-}100)} > {}^{PEO}T_{m(PU\text{-}5\text{-}100)} > {}^{PEO}T_{m(PU\text{-}2\text{-}100)}$. Effect of drying temperature; $^{PEO}T_{m(PU\text{-}2\text{-}60)} > {}^{PEO}T_{m(PU\text{-}2\text{-}100)}$, $^{PEO}T_{m(PU\text{-}5\text{-}60)} > {}^{PEO}T_{m(PU\text{-}5\text{-}100)}$, and $^{PEO}T_{m(PU\text{-}8\text{-}60)} > {}^{PEO}T_{m(PU\text{-}8\text{-}100)}$. ΔT_m is calculated as the absolute value of $^{PU\text{-}X}\Delta T_m = {}^{PU\text{-}X\text{-}60}T_m - {}^{PU\text{-}X\text{-}100}T_m$, where X indicates the molecular weight of the PEO used in kilo daltons. ΔT_m systematically increases with increasing soft segment molecular weight. This is related to the formation of α-complex crystals via confined crystallization of PEO within the subnanometer urea channels.

The changes in ${}^{PEO}T_m$ values as a function of soft segment molecular weight and annealing temperature are shown in Figure 5. ${}^{PEO}T_m$ values of the samples prepared at 60 °C are higher than those of their analogues prepared at 100 °C, meaning that the drying protocol comprising a thermal treatment at 100 °C results in a decrease in the ${}^{PEO}T_m$.

In addition, ΔT_m systematically increases with increasing soft segment molecular weight. This is directly related to the formation of α-complex crystals via confined crystallization of polyethylene oxide chains in subnanometer urea channels. As the PEO chain length increases, the thickness of the α-complex in the longitudinal direction, i.e., the channel length, which can be followed by its increasing melting point (${}^{\alpha}T_m$) given in Figure 7b, increases too in accordance with the one-dimensional (1D) nature of the α-complex. This indicates that lateral surface area, and thus, higher number of nucleation sites on the 1D threadlike cores of the complex also increases with increasing PEO chain length. In this respect, other PEO chains are driven to align in the longitudinal direction, i.e., in a parallel manner with the 1D α-complex, and strung together by the threadlike core. The increase in the thickness in the longitudinal direction with increasing PEO chain length gives rise to the decrease in the thickness in the radial direction with the same extent. For instance, as the formation of α-complex leads to a decrease in the radial thickness resulting in a decrease of 2 °C (${}^{PU\text{-}2}\Delta T_m$) in ${}^{PEO}T_m$ of the copolymer based on PEO-2000 soft segment (PU-2), this decrease (${}^{PU\text{-}8}\Delta T_m$) becomes three times higher for the copolymer based on PEO-8000 (PU-8), since the PEO chain length in PU-8 is three times higher than the one in PU-2.

***Micro-phase separation/mixing*:** The exotherms located at 119, 139 and 159 °C in Figure 1b are assigned to the micro-phase separation temperatures (T_{MST}) of PU-2-100, PU-5-100 and PU-8-100, respectively. The change in T_{MST} as a function of soft segment molecular weight is plotted in Figure 6. T_{MST} linearly increases with increasing soft segment molecular weight.

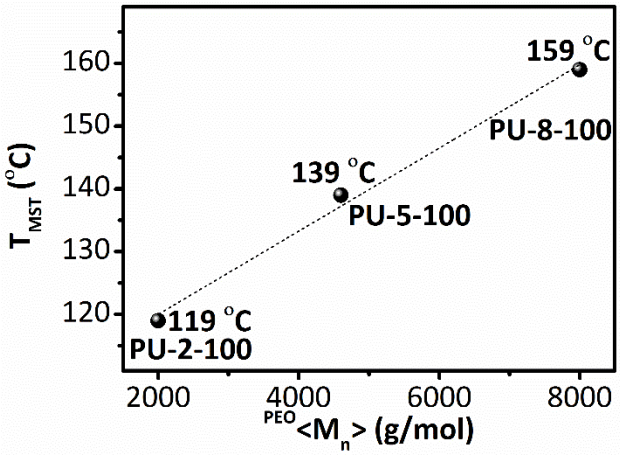

Figure 6. The change in T_{MST} as a function of soft segment molecular weight (SSMW).

In general, the micro-phase separation temperature in diblock copolymers has been reported to be dependent on the product χN as well as the content of the copolymer, where χ is referred as the Flory-Huggins interaction parameter and N is the

polymerization index. This is also applied for segmented copolymers like polyurethanes. As the soft segment molecular weight increases, the hard segment molecular weight increases too for achieving a constant weight fraction in terms of percent HS content. Therefore, the average sequence length increases too. In this respect, as suggested by Koberstein and Russell[38], if χ is inversely proportional to temperature, the effect of the increasing average sequence length would be to raise the T_{MST}. In general, this transition (T_{MST}) is followed by the micro-phase mixing (T_{MMT}) and/or the melting of micro-crystalline hard domains in polyurethanes. The presence of multiple endotherms is usually associated with either melting or mixing of phases with the different domain sizes. Consequently, it is crucial to understand the origins of such endothermic peaks observed at high temperatures. It is also of particular interest to address the two interrelated questions denoted as follow: *(I) Are these peaks solely formed by the heating effect during DSC scan? (II) Are they arisen from the thermal transitions of the phases, such as melting of the crystals, already existing in the samples?* To address this issue, the high temperature endotherms must be examined together with the micro-phase separation exotherm since, in such thermograms, the enthalpy changes of micro-phase separation (ΔH_{MST}) and micro-phase mixing (ΔH_{MMT}) processes are almost equal to each other. Therefore, it is reasonable to consider that the difference between these two enthalpy changes, which is defined as ${}^{\alpha}\Delta H = \Delta H_{MMT} - \Delta H_{MST}$, should be originated from the thermal transitions of the phases already existing in the samples. From this perspective, we attempt to understand the origins of the peaks observed at the high temperatures. Aforementioned, PU-2-100 shows an exotherm with a peak temperature of 119 °C and multiple endotherms with peak temperatures of 176, 184 and 192 °C in the high temperature region (Figure 1b). Interestingly, the peak temperatures vary with the same extent, i.e., the difference between two subsequent peak temperatures are equal to each other as described as follow: $T_{192} - T_{184} = T_{184} - T_{176} = 8$ °C, where the the subscripts represent the corresponding peak temperatures (Figure 7a). Therefore, it is reasonable to consider that PU-2-100 contains the α-complex crystals with three different sizes in three different "mixed" phase domains. For this material, ${}^{\alpha}\Delta H$ is calculated as 11.8±0.7 J/g_{PU} assuming that the respective three endotherms are arisen from melting of α-complex crystals with three different sizes, which simultaneously takes place with mixing of the phases in these domains. The ${}^{\alpha}\Delta H$ of 11.8±0.7 J/g_{PU} basically indicates the presence of a crystalline phase giving rise to the formation of such a difference between ΔH_{MMT} and ΔH_{MST} enthalpy changes. ${}^{\alpha}\Delta H$ values are also calculated as 15.4±0.5 and 16.9±0.6 J/g_{PU} for PU-5-100 and PU-8-100, respectively. It should be emphasized that ${}^{\alpha}\Delta H$ increases with increasing soft segment molecular weight. Moreover, there is a correlation between the peak temperatures of high temperature endotherms observed for the samples prepared at 100 °C with respect to the soft segment molecular weight (Figure 7b). If we assume three different hypothetical domain sizes (D_{α_1}, D_{α_2}, D_{α_3}) assigned for these three endotherms, one can easily see that the peak temperature linearly increases with increasing domain size (Figure 7a) since

the difference between two subsequent peak temperatures are equal to each other that can be defined as $\Delta^{\alpha}T_M = T_{192} - T_{184} = T_{184} - T_{176} = 8$ °C, where the the subscripts represent the corresponding peak temperatures. A similar trend is also observed as a function of soft segment molecular weight (Figure 7b). If we assume the peak at 192 °C as the main peak of $^{\alpha}T_M$ in PU-2-100, one can see that $^{\alpha}T_M$ linearly increases with increasing soft segment molecular weight, which can be described as $\Delta^{\alpha}T_M = {}^{\alpha}T_{PU\text{-}8\text{-}100} - {}^{\alpha}T_{PU\text{-}5\text{-}100} = {}^{\alpha}T_{PU\text{-}5\text{-}100} - {}^{\alpha}T_{PU\text{-}2\text{-}100} = T_{220} - T_{206} = T_{206} - T_{192} = 14$ °C.

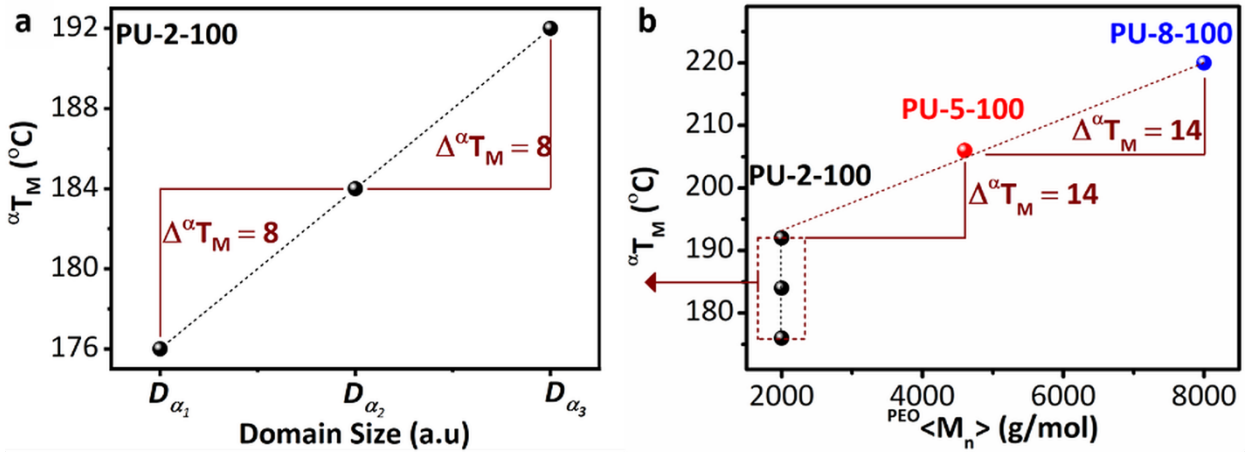

Figure 7. The change in $^{\alpha}T_M$ as a function of domain size for triple endotherms in PU-2-100 (a) and soft segment molecular weight (b).

3.3. X-ray diffraction

Figure 8-10 show X-ray diffractograms of the PU samples recorded at room temperature. Upon the results obtained from MDSC analyses along with a careful literature review, we considered that three different crystalline phases are likely to be formed in our materials. One of them is the crystalline PEO with a monoclinic unit cell[39-43], the other one is tetragonal urea crystals[44], and the third one is the PEO-Urea α-complex crystals with a trigonal unit cell[45-52]. The crystallographic data for these three crystal structures are well documented in the literature.[39–52] However, to the best of our knowledge, formation of the PEO-Urea α-complex crystals in segmented copolymers has not yet been reported.

Characteristic diffraction peaks of the monoclinic PEO crystals are mainly observed at 2θ values of 13.4°, 14.5°, 14.9°, 17.1°, 19.3°, 20.8°, 21.1°, 21.8°, 22°, 22.8°, 23.2°, 24.1°, 26.2°, 26.7°, 27.5° and 32.0° for (100), (021), (110), (101), (120), (031), (104), (102), (023), (112), (032), (130), (033), (131), (200) and (211) in the *hkl* index, respectively.[41] In this respect, the molecule bears seven repeating unit consisting of two helical turns (7_2-helix) over the length of 19.48 Å and the conformation depicts the four helical molecules (two right- and two left-handed helices) in one unit cell with the lattice parameters listed as a: 8.05 Å, b: 13.04 Å and c: 19.48 Å with β=125.4° (the oblique angle between the a- and c-axis). The orientation of the helix is along the [001] c-axis and chain folding follows the (120) planes. The (120) reflections (2θ=19.3°) taken along the [001] zone axis have information about interchain separations and chain conformations, whereas the (112)

reflections (2θ=23.2°) contains structural information along the c-axis, i.e., the helicity of PEO macromolecules.[42] Characteristic diffraction peaks of the tetragonal urea crystals are located at 2θ values of 22.1°, 24.6°, 29.3°, 31.6°, 35.5° and 37.1° for (110), (101), (111), (200), (210) and (201) crystal planes, respectively.[44] In addition, characteristic diffraction peaks of the PEO/Urea α-complex are reported to be at 2θ values of 13.6°, 16.7°, 19.3°, 21.6°, 25.8° and 27.4° for crystal planes of (101), (110), (200), (102), (112) and (202), respectively.[51]

Crystallographic details of PEO/Urea α-complex were reported by Chenite and Brisse.[45] This complex crystal belongs to the trigonal system, $P3_221$ space group, with unit cell dimensions of a=b=10.493 Å, c=9.134 Å, and γ=120°. As suggested by these authors, the urea molecules form pseudo-hexagonal channels and the walls of the channels are built by the hydrogen bonded urea molecules in this complex crystal. The channels are filled with PEO chains and the excess urea molecules that form a strongly hydrogen bonded complex. The PEO chains in this form is reported to adopt 4_1 helical conformation $(tgt)_4$, which is also referred as 4_1-helix, that is considered to be more squashed than the pure PEO (7_2-helix). This behavior was further confirmed by several studies in literature based on model compounds.[45–52]

Figure 8 shows XRD patterns obtained from PU-2-60 and PU-2-100. PU-2-60 only displays an amorphous halo, whereas PU-2-100 shows two sharp peaks at 19.3° and 23.3° and a fairly weak peak at 27.4° and 36.2°. The XRD pattern obtained for PU-2-60 is expected and in accordance with the results obtained from thermal analyses (Figure 1a), indicating that the sample is amorphous at room temperature as the melting endotherm observed in PU-2-60 is below room temperature. However, the XRD pattern of PU-2-100 is an unexpected result due to the following reasons: (*i*) The melting endotherm of PEO soft segment in PU-2-100 is below the room temperature (Figure 1b) that indicates an amorphous sample at room temperature like PU-2-60. Thus, these peaks are unlikely to be originated only from PEO soft segments. (*ii*) The hard segment model compounds are also found to be completely amorphous as demonstrated in Figure S2. Hence, the peaks are unlikely to be derived only from the hard segments either. (*iii*) Even if we assume that they are originated from pure crystalline hard domains formed by hydrogen bonded urea groups, the positions of these peaks, at least, should be similar to the ones reported for urea model compounds. However, this is not the case here. (*iv*) In addition, the peaks, at least at the first glance, are fairly similar to the ones typically assigned for the crystalline PEO rather than urea. (*v*) Nevertheless, they should be associated with the structures giving rise to the formation of multiple endotherms at high temperatures (Figure 1b).

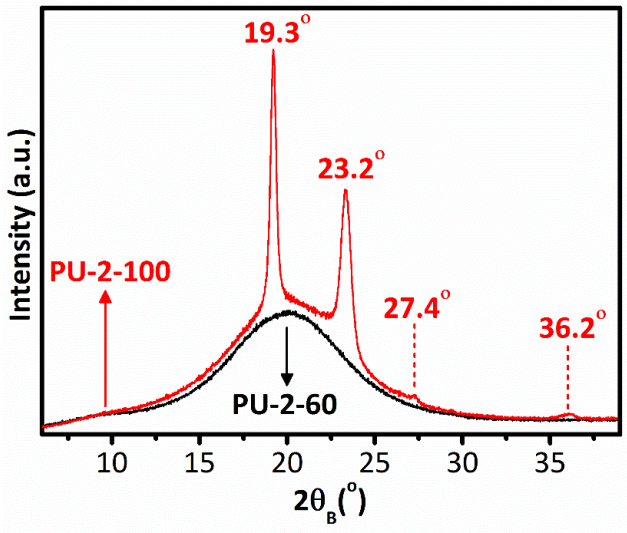

Figure 8. XRD patterns of PU-2-60 and PU-2-100.

We therefore consider that the peaks may be originated from a complex crystal structure involving both PEO and urea units. Upon a careful literature review, we have then found out that the peaks at 19.3° and 27.4° can indeed be arisen from PEO-Urea α-complex crystals. They mainly correspond to the crystal planes of (200) and (202), respectively. The intensity of the peak at 19.3° is significantly higher than that of the peak at 27.4° indicating a 1D structure in line with the corresponding crystal plane (200). Structural features of this complex crystal formed in ‘’host-guest’’ systems referred to as *PEO-Urea inclusion complexes* are well-documented in the literature. However, to the best of our knowledge, the question of whether this kind of complex crystal can form in PU copolymers containing PEO and urea units has not yet been addressed. Our results suggest that this, in fact, is possible.

There is also another strong peak at 23.3° (Figure 8). This peak is generally referred to as a characteristic peak of helical PEO chains assigned to (112) and/or (032) crystal planes representing the degree of helicity since it is not observed in the transplanar form.[41] Considering 7_2 helical nature of PEO chains in pure form, this peak can be an indicative of some “crystallized” PEO chains in the mixed phase placed in the immediate vicinity of threadlike cores of the α-complex. There is another peak at 36.2°, which is in the middle of two characteristic peaks of tetragonal urea crystals generally observed at 35.5° and 37.1° corresponding to the crystal planes of (210) and (201). The intensity of this peak is very similar to that of the peak located at 27.4°. Considering all the apparent peaks together, it is reasonable to envisage that 1D threadlike cores of the α-complex involving 4_1 helical PEO chains and hydrogen bonded urea molecules are surrounded by another crystalline layer of the mixed phase containing some “crystallized” PEO chains with 7_2 helical conformation and tetragonal urea crystals. In comparison to the tightly packed α-complex crystals, this crystalline layer is expected to be in a relatively more “disordered” state.

Figure 9 display XRD patterns of the PU copolymers based on PEO-4600 and PEO-8000 soft segments. On one hand, PU-5-60 displays the peaks located at 14.9°, 19.3°, 23.2° and 26.2°, respectively (Figure 9a). The peaks at 14.9°, 19.3° and 23.2° are also observed for PU-8-60 (Figure 9b). However, the peak located at 26.2° is not clearly visible for this sample. The intensities of the peaks at 19.3° and 23.2° are significantly higher than the ones observed at 14.9° and 26.2° for both PU-5-60 and PU-8-60. On the other hand, PU-5-100 shows the peaks at 13.6°, 14.6°, 15.2°, 19.3°, 23.2°, 25.8°, 26.2° and 27.2°, 29.4°, 30.8° and 36.2°, respectively (Figure 9a). Similarly, the peaks located at 13.6°, 14.5°, 15.1°, 19.3°, 21.1°, 22.0°, 23.2°, 25.8°, 26.2°, 27.2°, 27.7°, 30.8° and 36.2° are observed for PU-8-100 (Figure 9b). The intensities of the peaks at 19.3° and 23.2° are significantly higher than those of the other peaks in both of the samples. The peaks located at 21.1°, 22.0° and 27.7° are not clearly visible in the diffractogram of PU-5-100, whereas they become more apparent for PU-8-100.

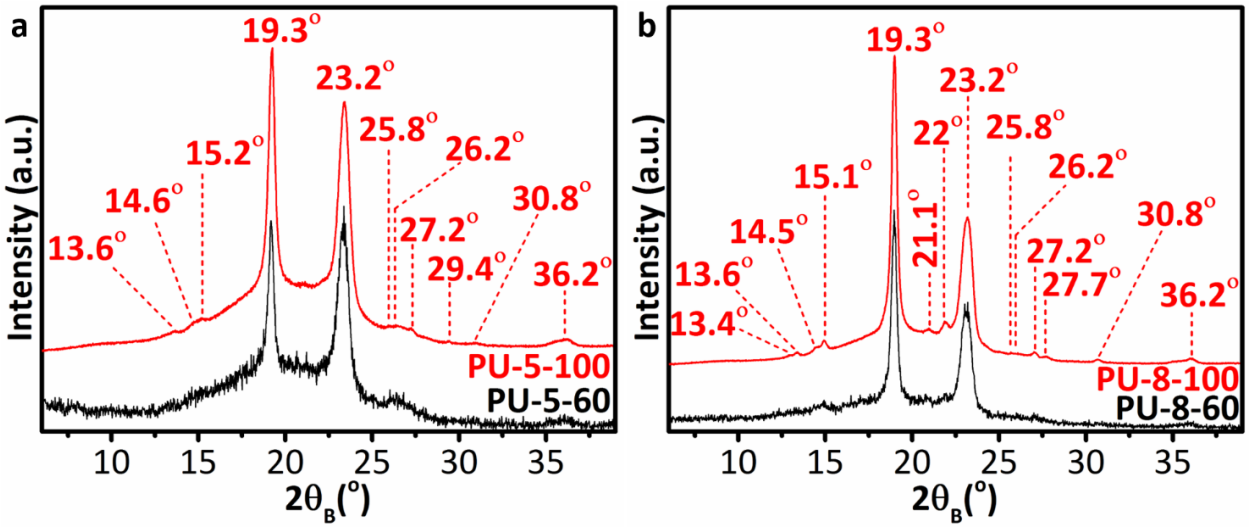

Figure 9. XRD patterns of (a) PU-5-60 and PU-5-100, and (b) PU-8-60 and PU-8-100.

The assignment of these peaks is provided in Figure 10 that also shows the comparison of the XRD patterns as a function of soft segment molecular weight. For PU-5-60 and PU-8-60 (Figure 10a), the peaks at 14.9°, 19.3° and 23.2° mainly correspond to the crystal planes of (110), (120) and (112), respectively.[41] The peak at and 26.2°, which is only visible for PU-5-60, is assigned to the crystal plane of (033). They are reported for 7_2 helical PEO chains and originated from the crystalline matrix phase in these two copolymers. These results are in a good agreement with the results obtained from MDSC analyses of these two copolymers suggesting that the endotherms located at 42.1 °C and 51.2 °C in the MDSC thermograms of PU-5-60 and PU-8-60 are originated from the melting of PEO soft segment crystals.

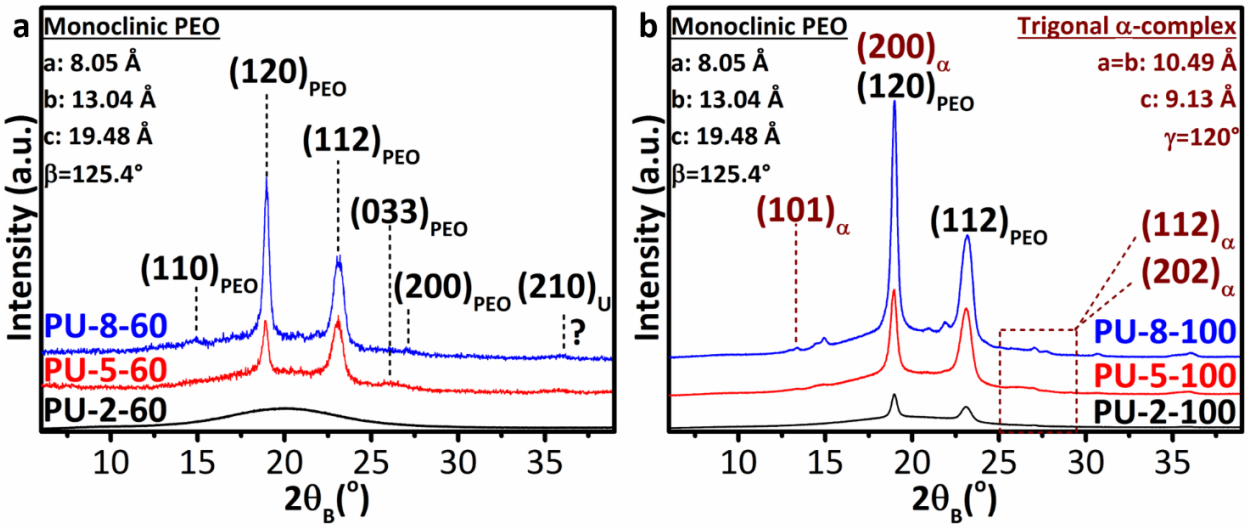

Figure 10. XRD patterns of (a) PU-2-60, PU-5-60 and PU-8-60, and (b) PU-2-100, PU-5-100 and PU-8-100 as a function of soft segment molecular weight.

For PU-5-100 and PU-8-100 (Figure 10b), the peaks located at 13.6° and 25.8° are originated only from the presence of PEO-Urea α-complex crystals. These two peaks are assigned to the crystal planes of (101) and (112) with d-spacings of 6.52 Å and 3.45 Å, respectively. Besides, the peaks resulted only from the presence of monoclinic PEO crystals are listed in the following along with the corresponding crystal planes and d-spacings: The peaks at 14.5°, 21.1°, 23.2° and 26.2° are assigned to the crystal planes of (021), (031), (112) and (033) with d-spacings of 6.11 Å, 4.21 Å, 3.83 Å and 3.40 Å, respectively. It should be noted that the peak at 23.2° can also be assigned to the crystal plane of (032) as reported in the literature.[41] More importantly, there are two mutual peaks located at 19.3° and 27.2°–27.7°, which are originated from the presence of both of the PEO-Urea α-complex and the PEO crystals. The peak located at 19.3° represents the crystal plane of (120) for the crystalline PEO, whereas it also corresponds to the crystal plane of (200) for PEO-Urea α-complex. If we assume that this peak is only resulted from the presence of PEO crystals, the peak intensities recorded for PU-5-100 and PU-8-100 samples should be lower than those of PU-5-60 and PU-8-60 since the corresponding crystallinity values of PU-5-60 and PU-8-60 are relatively higher than the ones recorded for PU-5-100 and PU-8-100, respectively. However, this is not the case in here. For this peak, the peak intensities in PU-5-100 and PU-8-100 are notably higher than the ones in PU-5-60 and PU-8-60, respectively. This result strongly suggests that the PEO-Urea α-complex crystals directly contribute to the total intensity of the peak located at 19.3° that mainly corresponds to the d-spacing of 4.59 Å. Therefore, it should be emphasized that this peak is originated from the presence of both of the PEO-Urea α-complex and the PEO crystals in both samples.

To provide a clear overview on the peaks located at 27.2°–27.7° as well as the other small peaks, a magnified view of the diffractogram obtained from PU-8-100 is representatively reproduced in Figure 11. It should be noted that most of the

small peaks highlighted in Figure 11 are also observed for PU-5-100. However, its diffractogram is not used in this figure for clarity. The peaks at 13.4, 14.5°, 15.1°, 21.1°, 22.0°, 26.2° (Figure 11) are arisen only from the presence of monoclinic PEO crystals. These peaks correspond to the crystal planes of (100), (021), (110), (104), (023), (033), respectively. The peaks at 13.6° and 25.8° corresponding to the crystal planes of (101) and (112) are originated only from the presence of PEO-Urea α-complex crystals. The peak expected to be located at 27.4°, which is assigned to the crystal planes of (202) and (200) for trigonal PEO-Urea α-complex and monoclinic PEO crystals, respectively, in the literature, seems to be splitted into two different peaks located at 27.2° and 27.7°. The d-spacings of these two peaks are 3.27 Å and 3.22 Å, respectively. Another small peak is observed at 30.8°. In this region, it is expected to see two characteristic peaks of crystalline urea, which are generally located at 29.3° and 31.6° corresponding to the crystal planes of (111) and (200), respectively. Thus, it is likely that the small peak at 30.8° is arisen from a combination of two characteristic peaks of crystalline urea. This might be due to the interactions between the PEO and urea groups. A similar combination is also observed for the peaks expected to be located at 35.5° and 37.1° in pure form as denoted in Figure 9. Instead of these two characteristic peaks corresponding to the crystal planes of (210) and (201) of urea crystals, there is a single peak at 36.2°, which is in the middle of those two.

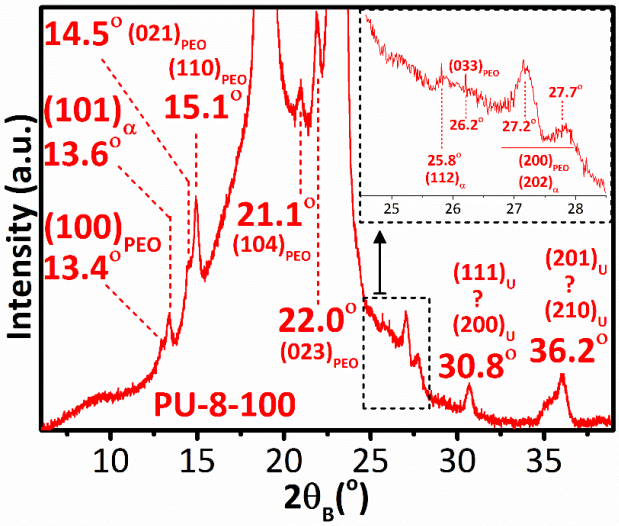

Figure 11. The small peaks representatively shown in the XRD pattern of PU-8-100.

Overall, the XRD results are in a good aggrement with the data obtained from MDSC analyses of the PU copolymers. These results mainly suggest that PU-2-60 is completely amorphous at room temperature, whereas PU-2-100 contains PEO-Urea α-complex crystals surrounded by another crystalline layer, which is formed by a mixed phase comprising some "crystallized" helical (monoclinic) PEO crystals and hydrogen-bonded (tetragonal) urea crystals (Figure 8). On the other hand, PU-5-60 and PU-8-60 contain monoclinic PEO crystals, whereas PU-5-100 and PU-8-100 comprise both trigonal

PEO-Urea α-complex crystals and monoclinic PEO crystals (Figure 9). The structure formation is basically governed by the bulk crystallization of the PEO chains in both PU-5-60 and PU-8-60, whereas it is mainly driven by the confined crystallization of the PEO chains in subnanometer urea channels in both PU-5-100 and PU-8-100, which is followed by the formation of monoclinic PEO crystals that are initially nucleated on the lateral surfaces of the α-complex crystals. Our interpretation has been only based on the peak positions so far. However, the positions of characteristic diffraction peaks of the crystalline PEO are very similar to those of the PEO-Urea α-complex crystal structure. We therefore consider that this should be supported by the quantitative analysis of the results in terms of crystallinity.

In an effort to quantify our results, the patterns over a specific angular range of 10°–40° were fitted using Origin® data processing software to a linear combination of a Lorentz function for the amorphous halo and Pearson functions for the crystalline peaks, which is a widely accepted fitting procedure for such materials in the literature.[41,53] The total crystallinity values of the samples were calculated as ${}^{XRD}\chi_c = [I_c / (I_c + I_a)]$, where I_c and I_a are the integrated intensity of all crystalline peaks and of the amorphous halo, respectively. The corresponding results are plotted in Figure 12.

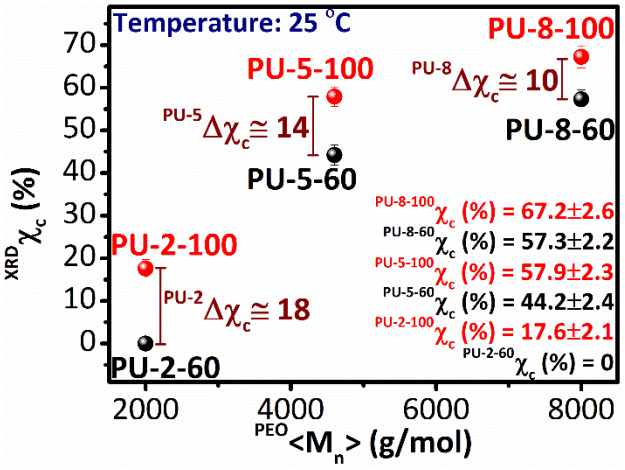

Figure 12. Total crystallinity values of the samples at 25 °C along with the percent increases arisen from the change in the drying temperature.

The ${}^{XRD}\chi_c$ values are calculated as 0%, 44.2% and 57.3% for PU-2-60, PU-5-60 and PU-8-60, respectively. As PU-2-60 displays an amorphous halo in its XRD pattern recorded at room temperature and an endotherm below the room temperature in its MDSC thermogram, it is reasonable to obtain the ${}^{XRD}\chi_c$ value as 0% for this sample. In addition, the ${}^{XRD}\chi_c$ values of PU-5-60 and PU-8-60 are in a good aggrement with ${}^{DSC}\chi_{c(SS)}$ values calculated from the total heat flow signals. The total crystalline fractions of the samples prepared at 60 °C (PU-2-60, PU-5-60 and PU-8-60) are equal to the crystalline fractions of the PEO soft segments since there is no apparent thermal transitions related to the hard segments in their MDSC thermograms (Figure 1a).

The ${}^{XRD}\chi_c$ values of PU-2-100, PU-5-100 and PU-8-100 are calculated as 17.6%, 57.9% and 67.2%, respectively. The ${}^{DSC}\chi_{c(PEO)}$ values of these samples, on the other hand, are determined as 0%, 34.6% and 41.4% respectively. One can see that the ${}^{XRD}\chi_c$ values are significantly different than ${}^{DSC}\chi_{c(PEO)}$ values for the samples prepared at 100 °C. This means that there is a significant contribution to the ${}^{XRD}\chi_c$ values, i.e. total crystallinity, of the samples (PU-2-100, PU-5-100 and PU-8-100), which must be arisen from the presence of another crystalline phase. We therefore believe that this result confirms the presence of the PEO-Urea α-complex crystals.

To provide a more detailed insight, ${}^{XRD}\chi_c$ is defined as ${}^{XRD}\chi_c = {}^{XRD}\chi_{c(PEO)} + {}^{XRD}\chi_{c(\alpha)}$, where ${}^{XRD}\chi_{c(PEO)}$ and ${}^{XRD}\chi_{c(\alpha)}$ correspond to crystalline fractions of the PEO and the PEO-Urea α-complex, respectively. Assuming the same standard deviation between ${}^{XRD}\chi_{c(PEO)}$ and ${}^{DSC}\chi_{c(PEO)}$ values observed for the samples prepared at 60 °C, which is arisen from the different experimental conditions between XRD and MDSC analyses, ${}^{XRD}\chi_{c(PEO)}$ values of PU-2-100, PU-5-100 and PU-8-100 are calculated as 0%, 35.1% and 42.1%, respectively. Since ${}^{PEO}T_m$ of PU-2-100 is also well below the room temperature (Figure 1b), the ${}^{XRD}\chi_{c(PEO)}$ value is denoted as 0% for this sample. Inserting these ${}^{XRD}\chi_{c(PEO)}$ values into the equation of ${}^{XRD}\chi_c = {}^{XRD}\chi_{c(PEO)} + {}^{XRD}\chi_{c(\alpha)}$, the corresponding ${}^{XRD}\chi_{c(\alpha)}$ values of PU-2-100, PU-5-100 and PU-8-100 are calculated as 17.6%, 22.8% and 25.1%, respectively. The ${}^{XRD}\chi_{c(\alpha)}$ value of PU-2-100 also includes the crystalline fraction of the mixed phase containing some "crystallized" PEO chains with 7_2 helical conformation and tetragonal urea crystals in line with the multiple endotherms detected by MDSC analyses (Figure 1b). Figure 12 also shows the difference in the total degree of room temperature crystallinity values ($\Delta\chi_c$) between the homologues samples prepared at 60 and 100 °C, i.e., PU-2-60 vs. PU-2-100, PU-5-60 vs. PU-5-100, and PU-8-60 vs. PU-8-100, which is induced by the change in the drying temperature and calculated as ${}^{PU\text{-}X}\Delta\chi_c = {}^{PU\text{-}X\text{-}100}\chi_c - {}^{PU\text{-}X\text{-}60}\chi_c$, where X represents the molecular weight of the PEO used in kilo daltons. The drying at 100 °C results in (approximately) 18, 14 and 10% increases in the room temperature total crystallinity values of PU-2, PU-5 and PU-8 copolymers, respectively (Figure 12).

3.4. Spectroscopy

ATR-IR is a simple but powerful tool to investigate the characteristic features of PEO/Urea α-complex crystalline structures. Characteristic absorption bands for α-complex were listed as 1360, 1342, 1277, 1248, 953 and 945 cm^{-1}.[48,51] From these key bands, the absorption bands at 1360, 1277, 1248 and 945 cm^{-1} are generally assigned to CH_2 wagging, CH_2 twisting, CH_2 rocking and C-O-C deformation perpendicular to the chain axis, respectively. Whereas the ones at 1342 and 953 cm^{-1} correspond to CH_2 wagging, CH_2 twisting and rocking conformation parallel to the chain axis.[48,51,54]

Since PEO and urea can also form various meta-stable complexes with different forms, the difference between the thermodynamically stable α-complex and the others is mainly followed by CH_2 wagging absorption band of amorphous PEO chains at 1352 cm^{-1}. This band has been reported to split into two bands at 1360 cm^{-1} and 1342 cm^{-1} as a direct result

of the formation of α-complex crystals.[46,48,51] This can be clearly seen when the ATR-IR spectra of PU-2-60 and PU-2-100 provided in Figure 13 are compared.

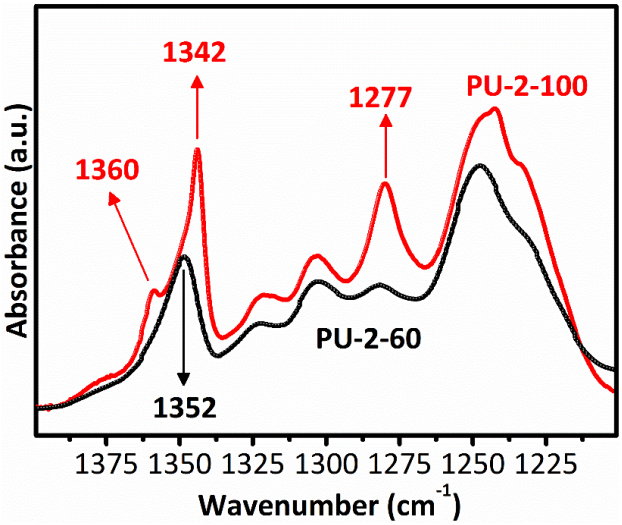

Figure 13. Comparative ATR-IR spectra of PU-2-100 (top spectrum) and PU-2-60 (bottom spectrum) in 1400–1200 cm^{-1} region.

When the polymer film is annealed at 60 °C, PEO chains are mainly in the amorphous state as evidenced by a single absorption band at 1352 cm^{-1} in the ATR-IR spectrum of PU-2-60, given in Figure 13. On the other hand, when it is prepared at 100 °C (PU-2-100), this band splits into two peaks centered at 1360 cm^{-1} and 1342 cm^{-1} as shown in Figure 13. Significant effect of PEO molecular weight on the formation of PEO/Urea α-complex can be seen in the 1400-1200 cm^{-1} region of the AT-IR spectra provided in Figure 14 for PU-2-100, PU-5-100 and PU-8-100. As the PEO molecular weight increases the peaks at 1360, 1342 and 1277 cm^{-1} showing the formation of PEO/Urea α-complex become much more pronounced.

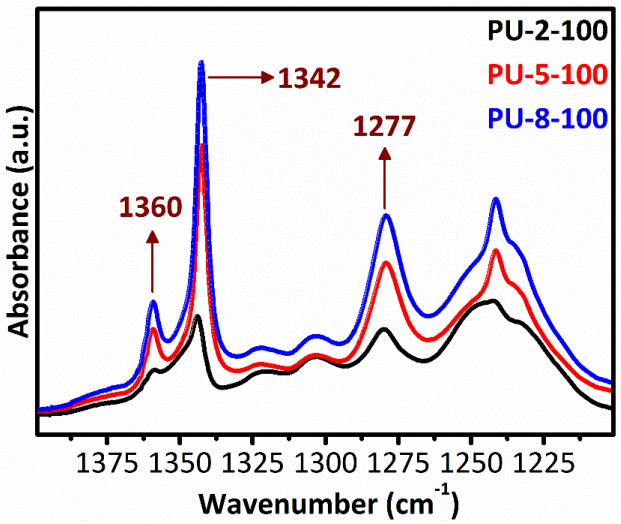

Figure 14. Comparative ATR-IR spectra of PU-8-100 (top spectrum), PU-5-100 (middle spectrum) and PU-2-100 (bottom spectrum) in 1400–1200 cm^{-1} region.

Formation of PEO/Urea α-complex can also be confirmed by Raman spectroscopy. Characteristic Raman bands of α-complex were listed as 1278, 1237, 862 and 845 cm^{-1}, whereas the peaks for the metastable complex were reported to be at 1308, 1259 and 845 cm^{-1} in the literature.[48] These bands are very similar to various crystalline forms of PEO and detailed conformational analysis and band assignments can be found in literature.[41,55-57] 1350-550 cm^{-1} region of the Raman spectra of PU-2-60 and PU-2-100 are reproduced in Figure 15. Formation of α-complex in PU-2-100 is indicated by the presence of well-defined peaks centered at 1278 and 1237 cm^{-1}, which are not observed in PU-2-60, and the sharp peak at 845 cm^{-1} that is significantly intense in PU-2-100 compared to PU-2-60 as shown in Figure 15. Characteristic absorption bands of the α-complex at 1278, 1237, 862 and 845 cm^{-1} are much more pronounced in the Raman spectra of PU-5-100 and PU-8-100, which are provided in Figure 16, together with PU-2-100 for comparison.

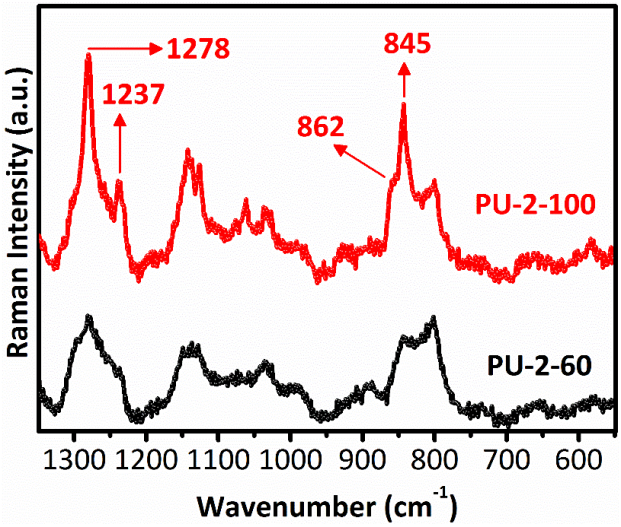

Figure 15. Raman spectra of PU-2-100 (top spectrum) and PU-2-60 (bottom spectrum) in 1350–550 cm^{-1} region.

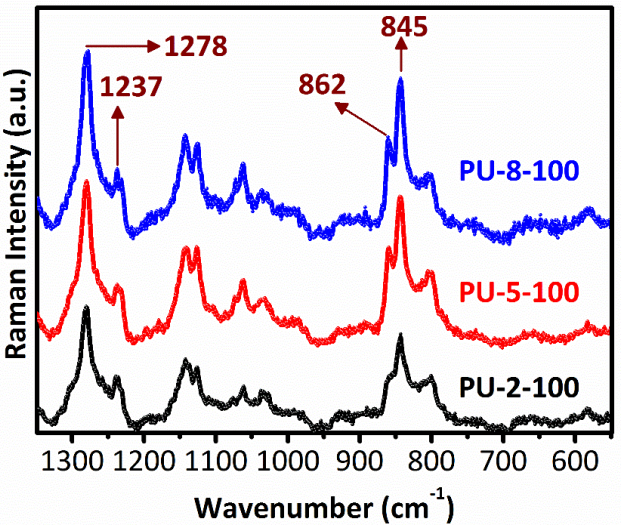

Figure 16. Raman spectra of PU-8-100 (top spectrum), PU-5-100 (middle spectrum) and PU-2-100 (bottom spectrum) in 1350–550 cm^{-1} region.

The spectroscopic data obtained from ATR-IR and Raman measurements are in accordance with the results obtained from MDSC and XRD analyses. Therefore, they can be evaluated together to provide more detailed structural insight into final room temperature morphologies of the PU copolymers under investigation, particularly for the ones prepared at 100 °C. Considering all these results together, it is interesting to note that PEO chains are adapted to two different secondary structures referred to as 4_1-helix and 7_2-helix. One of them (4_1-helix) is attributed to the PEO chains confined into the subnanometer urea channels as demonstrated by the presence of α-complex crystals, and the other one (7_2-helix) is assigned to the ones located in "bulk" PEO crystals. Both structures are stable in PU-5-100 and PU-8-100 at room temperature as both materials display two different melting endotherms well above the room temperature. For PU-2-100, the results basically suggest that the 4_1-helix in α-complex is stable at room temperature. Although the presence of multiple endotherms located at high temperatures (Figure 1b) and XRD peak located at 23.2° standing for the crystal plane of $(112)_{PEO}$ (Figure 8 and 10b), it is not easy to identify the room temperature stability of 7_2-helix in PU-2-100 as the melting endotherm belonging to the "bulk" PEO crystals is well below the ambient temperature. However, it is more interesting to determine other possible secondary structures in the PU copolymers under investigation, particularly PU-5-100 and PU-8-100, in addition to these two helical conformations. It is well-known that hydrogen bonded hard segments in PU copolymers –in general– form secondary structures identical to parallel/antiparallel (mostly antiparallel) β-sheets found in native structures like spider silk. Determining these structures in the presence of the two helical conformations demonstrated here would allow for a better understanding of intermolecular interactions and packing behavior between these sheets and helices. More importantly, it can provide a convenient framework to reconcile structural similarities between synthetic PU copolymers and protein based materials containing such secondary structures, such as spider silk.[58-66] Most recently, Johnson *et. al.*[67] investigated the influence of such secondary structures, α-helix and β-sheet in particular, on the mechanical properties of peptidic-polyurea hybrids based on 1,6-Hexamethylene diisocyanate (HDI) and poly(dimethylsiloxane) (PDMS, 2500 g/mol) incorporated by either poly(β-benzyl-L-aspartate) (PBLA) or poly(ε-carbobenzyloxy-L-lysine) (PZLY) peptide blocks with different sequence length in the form of "peptide–b–PDMS–b–peptide". ATR-IR studies conducted by these authors verified the existence of the desired secondary structures despite the simplicity of the polyureas. They observed mixtures of α-helix and β-sheet in those polymers consisting of longer peptidic segments. Besides, Tanaka *et. al.*[68] studied the secondary structures in highly crystallized ABA triblock copolymers (PBLA–PEO–PBLA) containing PEO blocks with M_n values of 11000 and 20000 g/mol. FT-IR results reported by these authors revealed the formation of a specific α-helix–7_2-helix–α-helix conformation. They did not observe the β-sheet conformation in as casted samples. But, they reported a structural change from an α-helix to a β-sheet conformation induced

by thermal treatment.[82] Forenamed natural design motifs, secondary structures, were also examined by Sogah's group[69,70] in silk-inspired multiblock copolymers containing poly(alanine–b–oxyethylene–b–alanine) triblock (M_n=823 and 1097 g/mol) comprising short PEG as a nonnative equivalence of the amorphous polypeptide domain of a spider silk.[69] They demonstrated the formation of β-sheets and their assembly into discrete nanostructures.[69] These secondary structures are usually followed by amide-I and amide-II regions of the ATR-IR spectra, which are provided in Figure 17a for the PU copolymers prepared at 100 °C. Although secondary structure characterization has been received particular attention in such polymeric systems containing peptidic units, the respective spectral regions (amide-I and amide-II) in non-peptide based PU copolymers like our materials have not been comprehensively analyzed in terms of those secondary structures. More specifically, despite the extensive base of PU literature, at least to the best of our knowledge, there are no reports where qualitative and quantitative assessment of secondary structures, and their effects on structure-property relationships of final materials have been systematically investigated as a function of critical design parameters like molecular weights of soft and hard segments. In the present work, we give an exclusive focus on the secondary structure determination as a part of our continuing efforts to provide more structural insight into the PU copolymers under investigation for a better understanding of their structure-property behavior. As shown in Figure 17a, at first glance, three different peaks are clearly visible at 1715–1711 cm^{-1}, 1633–1629 cm^{-1} and 1557–1550 cm^{-1} in the ATR-IR spectra of the samples. In polyurethane literature, these peaks are usually assigned to "ordered" urethane C=O, "ordered" urea C=O stretching and amide-II vibrations, respectively.[4] In line with this, quantification of these peaks is generally carried out to determine the extent of hard segment phase separation by calculating percent amounts of different carbonyl groups representing non-hydrogen bonded, hydrogen bonded, disordered, ordered structures.[71] However, such descriptions do not allow for the identification of the forenamed secondary structures in PU copolymers, which is of particular interest to understand the packing behavior in such complex materials along the multiple length scales.

In addition, as it can be seen in Figure 17a, the respective region is very broad due to overlapping of several peaks originated from the presence of different secondary structures. This suggests that the respective regions should be investigated in detail to provide more structural insight into the materials. To this end, a typical deconvolution procedure, which is summarized in Section 2.4, is carefully applied to provide a clear overview on the secondary structures in the PU copolymers prepared at 100 °C. Figure 17b representatively displays the deconvoluted amide-I peaks in the 1750–1600 cm^{-1} region of the ATR-IR spectra of PU-8-100. The corresponding results obtained from PU-2-100 and PU-5-100 are also provided in Figure S5 and S6, respectively.

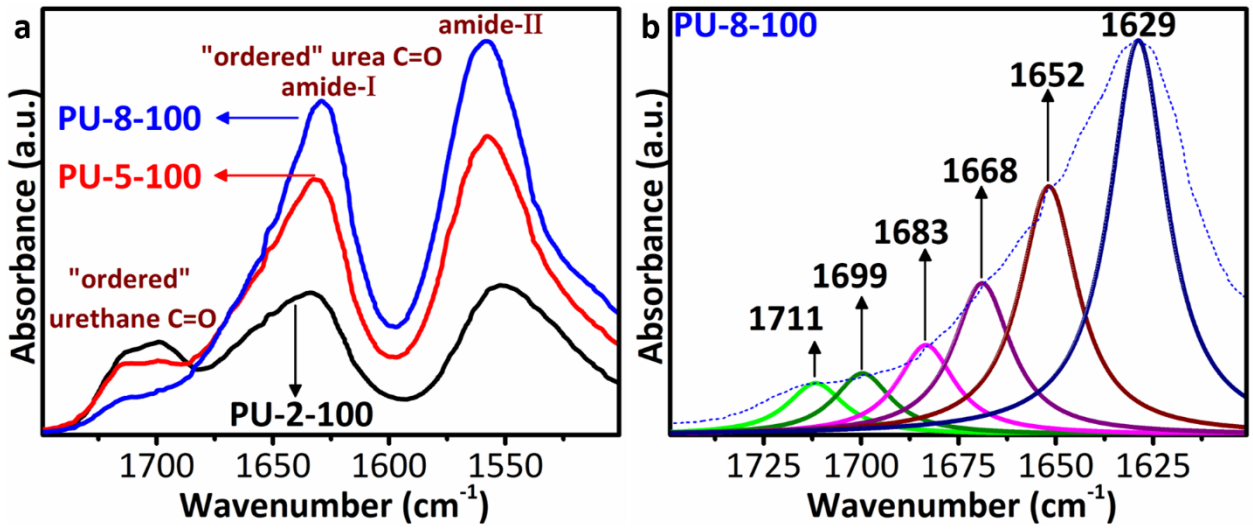

Figure 17. (a) Comparative ATR-IR spectra of PU-8-100 (top spectrum), PU-5-100 (middle spectrum) and PU-2-100 (bottom spectrum) in 1750–1500 cm^{-1} region. (b) Representative amide-I band deconvolution in PU-8-100: Six different peaks with peak maxima at 1711 cm^{-1} (β-turn$_{peak-I}$), 1699 cm^{-1} (β-turn$_{peak-II}$), 1683 cm^{-1} (β-turn$_{peak-III}$), 1668 cm^{-1} (β-sheet$_{peak-I}$), 1652 cm^{-1} (4_1-helix), and 1629 cm^{-1} (β-sheet$_{peak-II}$), respectively, are detected by deconvolution.

Six different peaks are found at 1715–1711 cm^{-1}, 1699 cm^{-1}, 1683 cm^{-1}, 1668 cm^{-1}, 1652 cm^{-1}, and 1633–1629 cm^{-1} for these three samples, i.e., PU-2-100, PU-5-100 and PU-8-100. The peaks at 1715–1711 cm^{-1} (at 1713 cm^{-1} for PU-2-100, at 1714 cm^{-1} for PU-5-100, at 1711 cm^{-1} for PU-8-100), 1699 cm^{-1} and 1683 cm^{-1} are originated from the presence of several different HMDI isomers, *such as trans,trans (E,E), trans,cis (E,Z) and cis,cis (Z,Z)*. HMDI isomers affect the packing behavior in the solid state. This in turn restricts the formation of the well-ordered hydrogen bonded structures in the PU copolymers.[71] Therefore, it is reasonable to consider that these three peaks mainly represent the monodentate hydrogen bonded structures. However, for these three peaks, the relative hydrogen bonding strength is different than each other. Considering the peak positions, it should be noted that the peak at 1683 cm^{-1} represents monodentate, but relatively well-ordered, hydrogen bonded structure (relatively stronger hydrogen bonding) compared to the peaks at 1699 cm^{-1} and 1715–1711 cm^{-1}. In other words, degree of imperfection in monodentate hydrogen bonding for the structures giving rise to the formation of these three peaks can be listed as follow: 1715–1711 cm^{-1} > 1699 cm^{-1} > 1683 cm^{-1}. In terms of secondary structures, we consider that these peaks can be assigned to β-turns since they are mainly formed by monodentate hydrogen bonds, and create loops at the chain ends. The peaks at 1668 cm^{-1} and 1633–1629 cm^{-1} (at 1633 cm^{-1} for PU-2-100, at 1631 cm^{-1} for PU-5-100, at 1629 cm^{-1} for PU-8-100) are assigned to antiparallel β-sheets, whereas the peak at 1652 cm^{-1} is mainly attributed to 4_1-helix. The antiparallel β-sheets are formed by the bidentate hydrogen bonded highly ordered urea molecules on the walls of the channels, whereas the excess urea molecules inside the channels adapt to 4_1-helix conformation as well as confined PEO chains. In accordance with this, characteristic amide-II peaks of the 4_1-helix and β-sheet secondary structures are also detected at 1557–1550 cm^{-1} (4_1-helix), 1535 cm^{-1} (β-sheet) and 1515 cm^{-1} (β-sheet),

respectively, by the deconvolution. The corresponding results are provided in Figure S7-S9. Similar results are obtained in the literature.[72] It should be emphasized that the peak around 1652 cm^{-1} is usually assigned to several helical structures, such as α-helix, 3_1-helix, for different materials. This suggests that the respective peak should be particularly examined for each system. In our case, the peak at 1652 cm^{-1} is attributed to 4_1-helix for the PU copolymers under investigation as it is also characterized by a series of experiments in the present study.

On the other hand, the deconvolution allows for quantitative assessment of the secondary structures listed above. Figure 18 and 19 display the fractions of the secondary structures as a function of soft segment molecular weight. In a general form, the fraction is defined as follow: ${}^{s}\phi = {}^{s}A_{peak} / A_{total}$, where s, ${}^{s}A_{peak}$, and A_{total} illustrate the secondary structure, the area under the respective peak and the total area under the cumulative peak, respectively.

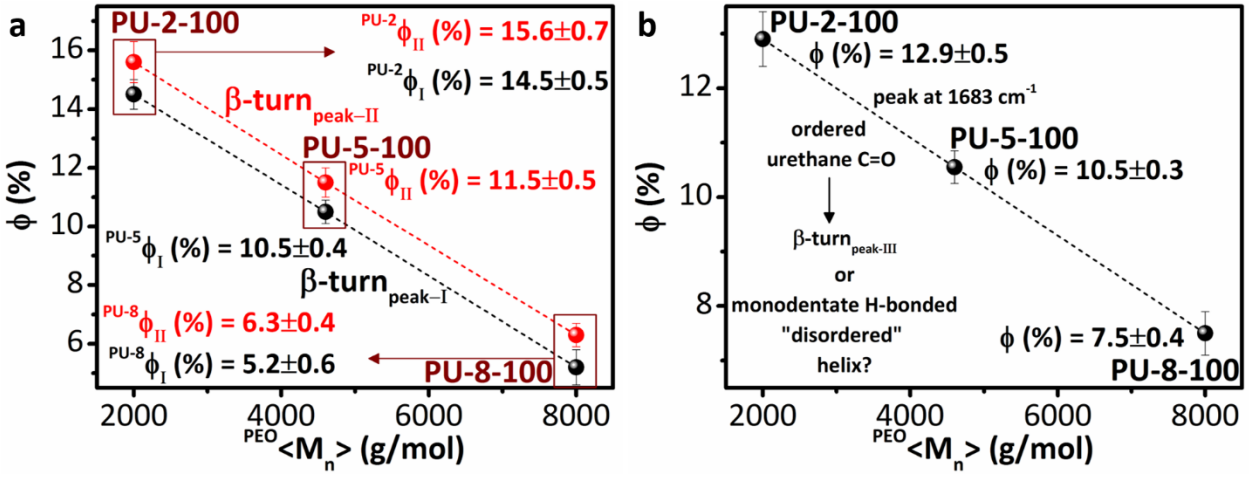

Figure 18. Fractions (ϕ) of the secondary structures as a function of soft segment molecular weight: (a) Fractions of β-$turn_{peak\text{-}I}$ (1715–1711 cm^{-1}) are calculated as ${}^{PU\text{-}2}\phi_I$ = 14.5%, ${}^{PU\text{-}5}\phi_I$ = 10.5%, ${}^{PU\text{-}8}\phi_I$ = 5.2%. Fractions of β-$turn_{peak\text{-}II}$ (1699 cm^{-1}) are determined as ${}^{PU\text{-}2}\phi_{II}$ = 15.6%, ${}^{PU\text{-}5\text{-}100}\phi_{II}$ = 11.5%, ${}^{PU\text{-}8\text{-}100}\phi_{II}$ = 6.3%. (b) Fractions of β-$turn_{peak\text{-}III}$ (1683 cm^{-1}) are calculated as 12.9%, 10.5% and 7.5% for PU-2-100, PU-5-100 and PU-8-100, respectively.

The peaks at 1715–1711 cm^{-1} (β-$turn_{peak\text{-}I}$), 1699 cm^{-1} (β-$turn_{peak\text{-}II}$) and 1683 cm^{-1} (β-$turn_{peak\text{-}III}$) are assigned to β-turns secondary structures. The total β-turn fraction is defined as ${}^{\beta\text{-}turn}\phi_{PU\text{-}X\text{-}100} = {}^{\beta\text{-}turn\text{-}peak\text{-}I}\phi_{PU\text{-}X\text{-}100} + {}^{\beta\text{-}turn\text{-}peak\text{-}II}\phi_{PU\text{-}X\text{-}100} + {}^{\beta\text{-}turn\text{-}peak\text{-}III}\phi_{PU\text{-}X\text{-}100}$ where X represents <M_n> of the PEO in kilodaltons. ${}^{\beta\text{-}turn\text{-}peak\text{-}I}\phi_{PU\text{-}X\text{-}100}$ and ${}^{\beta\text{-}turn\text{-}peak\text{-}II}\phi_{PU\text{-}X\text{-}100}$ are equal to ${}^{PU\text{-}X}\phi_I$ and ${}^{PU\text{-}X}\phi_{II}$ values denoted for β-$turn_{peak\text{-}I}$ and β-$turn_{peak\text{-}II}$ in Figure 18a, respectively, whereas ϕ values in Figure 18b represents ${}^{\beta\text{-}turn\text{-}peak\text{-}III}\phi_{PU\text{-}X\text{-}100}$ for β-$turn_{peak\text{-}III}$. It should be noted that β-$turn_{peak\text{-}III}$, the peak at 1683 cm^{-1}, is also referred to as "monodetate hydrogen bonded and/or disordered helix" in the literature.[72] Due to this reason, its relationship with PEO molecular weight is provided in a separate plot (Figure 18b) and its assignment is denoted with a "question mark". The β-$turn_{peak\text{-}I}$ fractions of PU-2-100, PU-5-100 and PU-8-100 are calculated as 14.5%, 10.5% and 5.2%, whereas their β-$turn_{peak\text{-}II}$ fractions are determined as 15.6%, 11.5% and 6.3%, respectively (Figure 18a). The β-$turn_{peak\text{-}III}$ fractions of these three samples (PU-2-100, PU-5-100 and PU-8-100) are calculated as 12.9%, 10.5% and 7.5%, respectively (Figure 18b).

Accordingly, their total β-turn fractions are determined as $^{\beta\text{-turn}}\phi_{PU\text{-}2\text{-}100}$ = 43%, $^{\beta\text{-turn}}\phi_{PU\text{-}5\text{-}100}$ = 32.5% and $^{\beta\text{-turn}}\phi_{PU\text{-}8\text{-}100}$ = 19%. As shown in Figure 18, $^{\beta\text{-turn-peak-I}}\phi$, $^{\beta\text{-turn-peak-II}}\phi$, $^{\beta\text{-turn-peak-III}}\phi$, and thus, $^{\beta\text{-turn}}\phi$ linearly decreases with increasing soft segment molecular weight (SSMW) since the number of chain ends decreases with increasing SSMW.

In contrast, the fractions of both 4_1-helix (Figure 19a) and β-sheet (Figure 19b) secondary structures linearly increase with increasing SSMW (Figure 19). This is due to the fact that increasing SSMW also means increasing hard segment molecular weight, and thus, increasing number of urea molecules that can participate in the secondary structure formation. The 4_1-helix fractions ($^{4_1\text{-helix}}\phi$) of PU-2-100, PU-5-100 and PU-8-100 are calculated as 19%, 22.5% and 27% (Figure 18a), whereas their β-sheet fractions ($^{\beta\text{-sheet}}\phi$) are determined as 38%, 45% and 54%, respectively (Figure 19b).

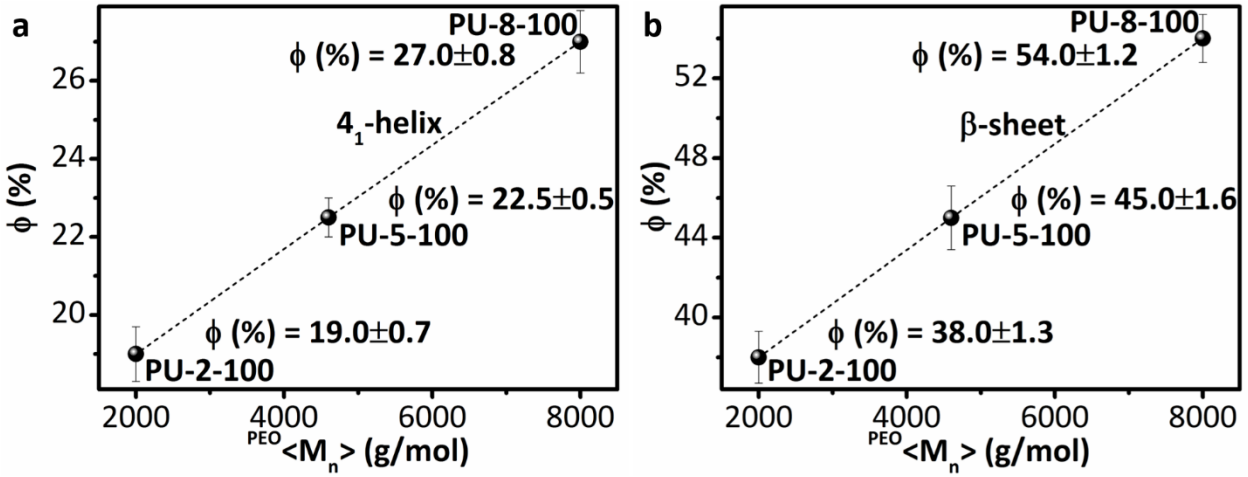

Figure 19. Fractions (ϕ) of the secondary structures as a function of soft segment molecular weight: (a) Fractions of the 4_1-helix: $^{4_1\text{-helix}}\phi_{PU\text{-}2\text{-}100}$ = 19%, $^{4_1\text{-helix}}\phi_{PU\text{-}5\text{-}100}$ = 22.5%, $^{4_1\text{-helix}}\phi_{PU\text{-}8\text{-}100}$ = 27%. (b) Fractions of the β-sheet: $^{\beta\text{-sheet}}\phi_{PU\text{-}2\text{-}100}$ = 38%, $^{\beta\text{-sheet}}\phi_{PU\text{-}5\text{-}100}$ = 45%, $^{\beta\text{-sheet}}\phi_{PU\text{-}8\text{-}100}$ = 54%.

The $^{4_1\text{-helix}}\phi$ values are calculated as the area under the peak at 1652 cm^{-1} divided by the area under the cumulative peak ($^{4_1\text{-helix}}\phi = A_{1652} / A_{total}$). Likewise, the $^{\beta\text{-sheet}}\phi$ values are calculated as the total area under the peaks at 1668 cm^{-1} and 1629 cm^{-1} divided by the area under the cumulative peak ($^{\beta\text{-sheet}}\phi = (A_{1668} + A_{1629}) / A_{total}$). As a part of the α-complex crystals, the 4_1-helix is also the conformation of the excess urea molecules inside the channels that adapt to the same conformation with the confined PEO chains within the channels. The β-sheet, on the other hand, is the conformation of the well-ordered urea molecules on the channel walls of the α-complex crystals. The quantitative results obtained from the deconvolution also support the presence of the α-complex crystals and their structural features. Based on the secondary structures, the superstructure of the α-complex crystals can be defined as the combination of three different layers: one internal (4_1-helix) and two external layers, i.e., the channel walls (β-sheet). Based on this three layer model, the total fraction of the α-complex crystals can be calculated as $^{\alpha\text{-complex}}\phi = [^{4_1\text{-helix}}\phi + (^{\beta\text{-sheet}}\phi / 2)] / 2$. Using this equation, $^{\alpha\text{-complex}}\phi$ values of PU-2-100, PU-5-

100 and PU-8-100 are determined as 19%, 22.5% and 27%, respectively. The $^{\alpha\text{-complex}}\phi$ values are in a good agreement with the $^{XRD}\chi_{c(\alpha)}$ values, which are calculated as 17.6%, 22.8% and 25.1% for PU-2-100, PU-5-100 and PU-8-100, respectively.

3.5. Microscopy

Microscopic studies of the samples were performed by OM and AFM techniques. Figure 20 shows OM images of PU-2-60 and PU-2-100 recorded at room temperature. As an expected result, PU-2-60 does not display any micro-structural feature since it is completely amorphous at ambient temperature (Figure 20a). This is also confirmed by AFM studies (Figure S10a). In line with this, the AFM phase image recorded with a scan size of 200x200 nm displays typical nanoscale morphology comprising dissolved hard segments in the soft matrix (Figure S10b). These results are in an excellent aggrement with the results obtained from MDSC, XRD, FT-IR and Raman spectroscopy.

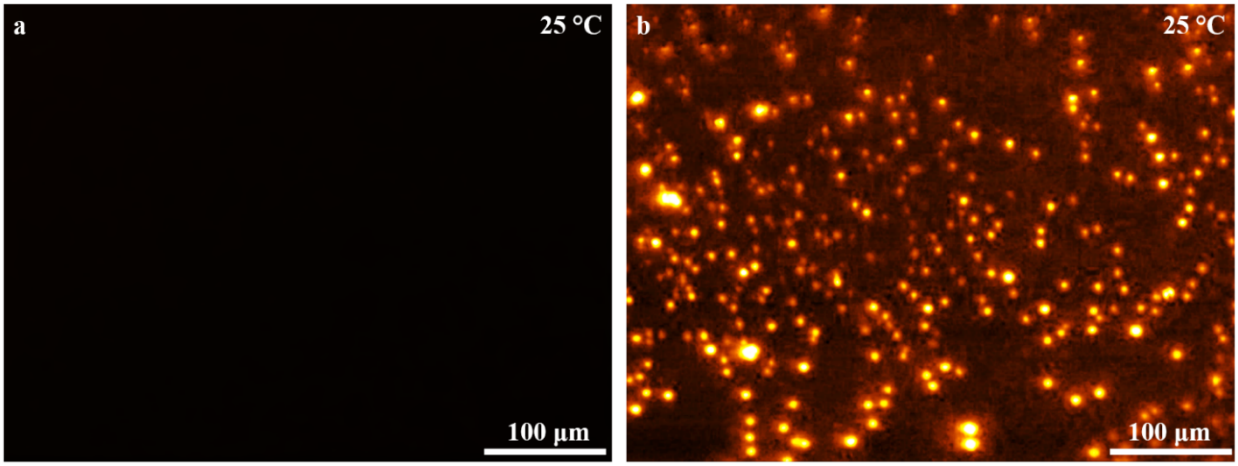

Figure 20. Optical microscope images of (a) PU-2-60 and (b) PU-2-100 at 25 °C.

As shown in Figure 20b, PU-2-100 shows microcrystalline domains distributed in an amorphous matrix. This observation provides a convenient framework to examine the origins of multiple high temperature endotherms observed in the MDSC thermograms. As the melting point of PEO crystals is below room temperature, the apparent crystalline phases in PU-2-100 should be related to the α-complex crystals giving rise to the formation of the high temperature endotherms. To clearly identify the form of microcrystalline domains, a high magnification image of one of the microcrystalline domains is also presented in Figure 21a. These results are of importance from two different perspectives: Firstly, the presence of microcrystals in the image of PU-2-100 recorded at room temperature basically proves that, at least, one of the multiple endotherms at high temperatures are not formed during the MDSC heating scan. Secondly, the apparent crystal shape also confirms our claim about the presence of the α-complex crystals. If we assume that one of the high temperature endotherms is originated from the presence of “pure” micro-crystalline hard domains solely formed by hydrogen-bonded hard segments, one should expect to see some needle-like structures as the hard segments mainly consist of urea groups.

However, this is not the case here. This mainly suggests that at least one of the endotherms at high temperatures is due to the melting of a crystalline phase already present in the material. Considering the apparent shape of the crystals along with the data obtained from XRD, ATR-IR and Raman spectroscopy measurements, this phase is considered to be formed by the α-complex crystals.

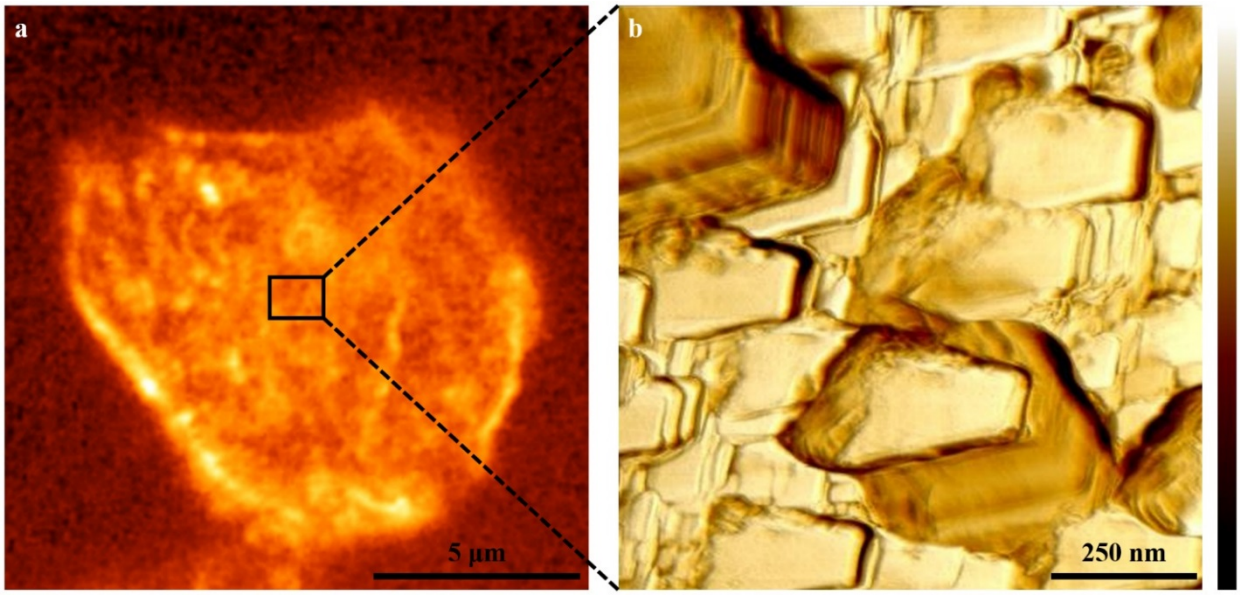

Figure 21. Morphology of PEO-Urea α-complex crystals as demonstrated by the optic microscope (a) and AFM phase (b) images along the multiple length scales.

In this respect, one can envisage two plausible scenarios: (I) These three endotherms might be originated from the melting of the α-complex crystals with three different domain sizes. (II) The two of the three endotherms, most probably the ones at 176 °C and 184 °C, might be arisen from the melting/micro-phase mixing of ordered hard domains formed by micro-phase separation process characterized with a peak temperature of 119 °C during the MDSC heating scan. However, one of them, most probably the one at 192 °C, is originated from the melting of a crystalline phase that already exists in the material as observed by OM and AFM (Figure 20b and 21). We believe that the first scenario is relatively more plausible as presented in Figure 7a.

The nanoscale phase morphology comprising a stack of hexagonal nanoplatelets shown in Figure 21b is in a good agreement with the literature. PEO molecular weight dependent morphologies of single crystals of the PEO/Urea α-complex in the range of 1000 to 100000 g/mol were analyzed using scanning electron microscopy by Chenite and Brisse.[45] The authors suggested that, for the high M_w values, the morphology is more likely to be a stack of hexagonal platelets rather than that of elongated pseudo-hexagonal prisms with very smooth faces which is mainly accounted for low molecular weight compounds. Considering the M_w of PU-2-100 (106000 g/mol), our results are in a good agreement with the observations made by Chenite and Brisse.

Upon these observations on the copolymer based on PEO-2000 soft segment, it is reasonable to consider that the structure formation in the material prepared at 60 °C (PU-2-60) is mainly governed by the lateral packing[73-75] of the bidentate H-bonded urea groups from molecular level to nanoscale. In general, the lateral packing results in fibrillar phase separated morphologies comprising an infinite stack of 1D H-bonded structures. This mechanism is also effective in PU-2-60, but only up to a certain length scale. The apparent nanoscale features therefore begin to dissappear beyond this length scale (Figure S10a) and they are no longer visible at larger length scales (Figure 20a). On the contrary, when the samples are prepared at 100 °C, the structure formation is mainly driven by the confined crystallization of the PEO chains in subnanometer urea channels giving rise to the formation of the thermodynamically stable α-complex crystals. This is because both soft and hard segments have sufficient mobility to form the most stable conformation via strong intermolecular hydrogen bonding between the PEO ether oxygens and the urea N-H groups. Hence, they are cooperatively assembled into the tightly packed trigonal form with minimum free energy. Similar mechanism is also reported for the respective model compounds.[48]

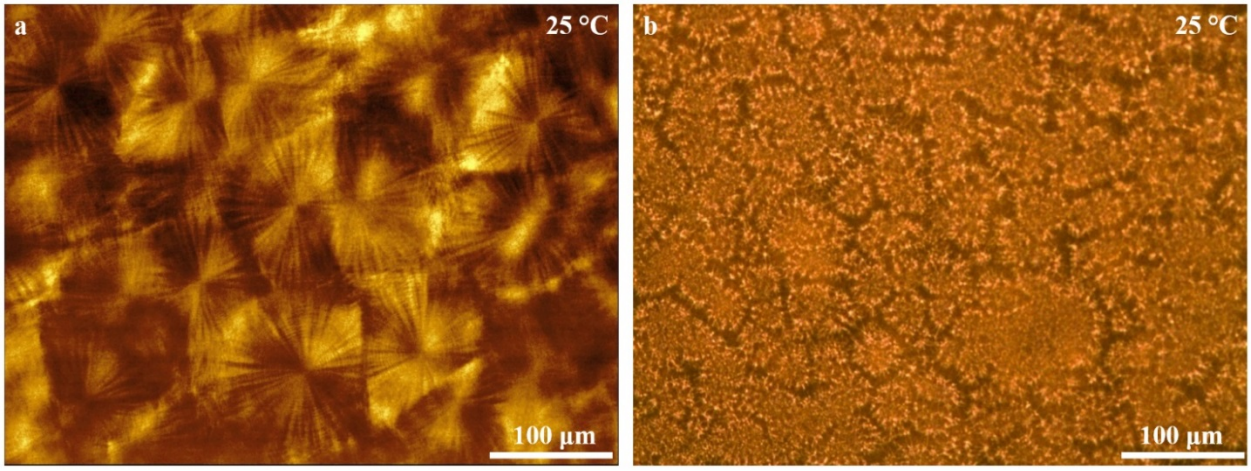

Figure 22. Optical microscope images of (a) PU-8-60 and (b) PU-8-100 at 25 °C.

The OM images of PU-8-60 (Figure 22a) and PU-8-100 (Figure 22b) recorded at room temperature are provided in Figure 22. On one hand, The OM image of PU-8-60 (Figure 22a) shows a typical spherulitic morphology of crystalline PEO with well-defined grain boundaries. As the formation of this structure is well-known in the literature, it will not be further discussed here. On the other hand, a geometrically confined crystalline morphology is observed for PU-8-100 (Figure 22b). This poses the question of how the confined crystallization of the PEO chains in the subnanometer urea channels does relate to the geometric confinement at the microscopic level. Before getting into this discussion, we should note that the morphologies presented for PU-8-60 and PU-8-100 represent the ones observed in PU-5-60 and PU-5-100, respectively. Furthermore, the presence of the α-complex crystals in PU-5-100 and PU-8-100 is also evidenced by the microscopic

analyses at a temperature (60 °C) above the melting points of PEO crystals as representatively shown in Figure S11. We can therefore conclude that both the monoclinic PEO and the trigonal α-complex crystals present in both PU-5-100 and PU-8-100 at ambient temperature.

However, this conclusion poses the question of how the final room temperature morphology given in Figure 22b is formed in the copolymers comprising both PEO and PEO-Urea α-complex crystals. To address this issue, AFM is used to examine the phase morphologies at smaller length scales. For both PU-5-100 and PU-8-100, a "beads on a string" type nanoscale morphology consisting of compact globular domains is observed. An AFM image recorded on PU-8-100 is representatively shown in Figure 23. Each globular domain is isotropically distributed at nanoscale. The average size of a globular domain of PU-8-100 is 48±4 nm, whereas that of PU-5-100 is 25±3 nm. This means that each globular domain consists of tightly packed secondary structures demonstrated above (7_2-helix, 4_1-helix and β-sheet). However, the question of which forces drive the formation of these globular domains with well-defined internal secondary structures still remains to be addressed.

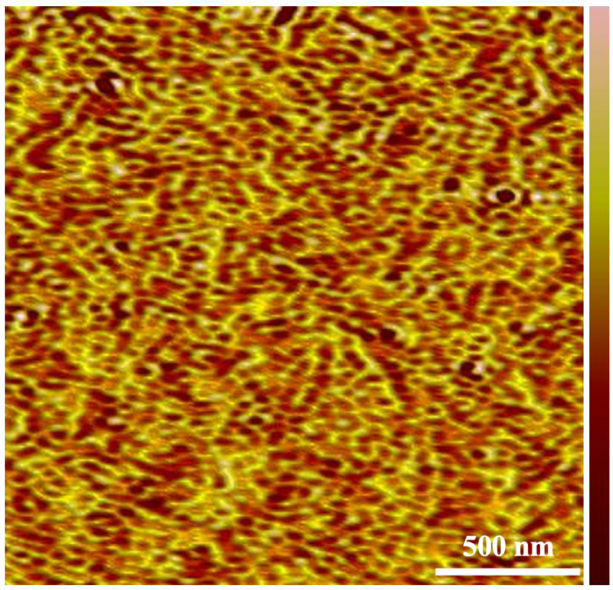

Figure 23. The "beads on a string" type morphology observed in PU-8-100 along the multiple length scales as demonstrated by the AFM phase image with a scale bar of 500 nm.

In principle, any self-avoiding flexible polymer chain would form a great number of secondary structures since it is basically driven to become more and more compact through any attractive force among the chain monomers.[76] This means that the structure formation in compact polymers is mainly related to the severity of steric constraints.[76] This steric principle of organization can provide a plausible explanation for why the samples dried at 100 °C are more compact than the ones dried at 60 °C. We basically have more steric constraints, i.e., geometric confinement, in the samples dried at 100 °C as compared to the ones dried at 60 °C since we have two mechanisms in which we have geometric confinement effects, i.e., the formation of PEO-Urea α-complex crystals and the "bulk" crystallization of PEO segments in the former, whereas we

have only one of them, i.e. the "bulk" crystallization of PEO segments, in the latter. The only notable geometric confinement arisen from the "bulk" crystallization of PEO segments is the acquirement of the *trans-gauche-trans* (*ttg*) conformation in the ethylene oxide units in the crystalline PEO soft domains with helical conformation (7_2-helix). This gives rise to a decrease in the conformation entropy. In addition, the oxygen atoms in these ethylene oxide units reside in the core of the helix surrounded by hydrophobic methylene groups[40] due to the presence of packed antiparallel helical strands with opposing handedness. This leads to hydrophobic core development in the materials. The formation of PEO-Urea α-complex crystals, on the other hands, brings more steric constraints as it comprises confined crystallization of PEO within the subnanometer urea channels, "ordering" of hydrogen bonded urea groups with anti-parallel β–sheet conformation on the walls of the channels. Similar to the "bulk" crystallization case, the acquirement of the $(tgt)_4$ conformation in the ethylene oxide units in the confined helical PEO crystals (4_1-helix) also leads to a decrease in the conformation entropy. This is a relatively more substantial decrease since 4_1-helix is more squashed than 7_2-helix. The formation of hydrogen bonded urea groups with anti-parallel β–sheet conformation contributes to the reduction of conformational entropy. Two mechanisms take place in the samples dried at 100 °C along with the "bulk" crystallization of PEO. Hence, the geometric confinement is -overall- more severe in these samples. The severity of steric constraints enables them to collapse to highly compact globular domains with large amounts of tightly packed secondary structures. This may be of interest in designing synthetic replica of certain proteins with specific internal architectures.

3.6. Tensile properties

Stress-strain curves of the PU copolymers are provided in Figure 24. PU-2 based samples display a well-defined elastomeric behavior while PU-5 and PU-8 based films show a typical elasto-plastic behavior with a distinct initial elastic response followed by yielding, softening, hardening and then failure. This is because the soft segment in PU-2 is completely amorphous and (due to its T_g) highly mobile at room temperature whereas it is semi-crystalline in both PU-5 and PU-8.

Significant differences are observed in the tensile behavior of homologous PUs regarding drying temperature. The drying at 100 °C results in dramatic improvements in mechanical properties of all the copolymers under investigated. The results obtained from tensile tests are summarized in Table 3. As compared to PU-2-60, PU-5-60 and PU-8-60, 276, 208 and 84% increases in elastic modulus (E), 13.6, 56.4 and 118% increases in ultimate tensile strength (σ_{max}), 18.6, 31.3 and 63.8% increases in elongation at break (ε) and 93.6, 123 and 213% increases in toughness (W) are obtained in PU-2-100, PU-5-100 and PU-8-100, respectively. In line with this, yield strengths (σ_y) of PU-5-100 and PU-8-100 are 103 and 72% higher than those of PU-5-60 and PU-8-60, respectively. No distinct yield is observed for PU-2 based samples due to their well-defined elastomeric behavior.

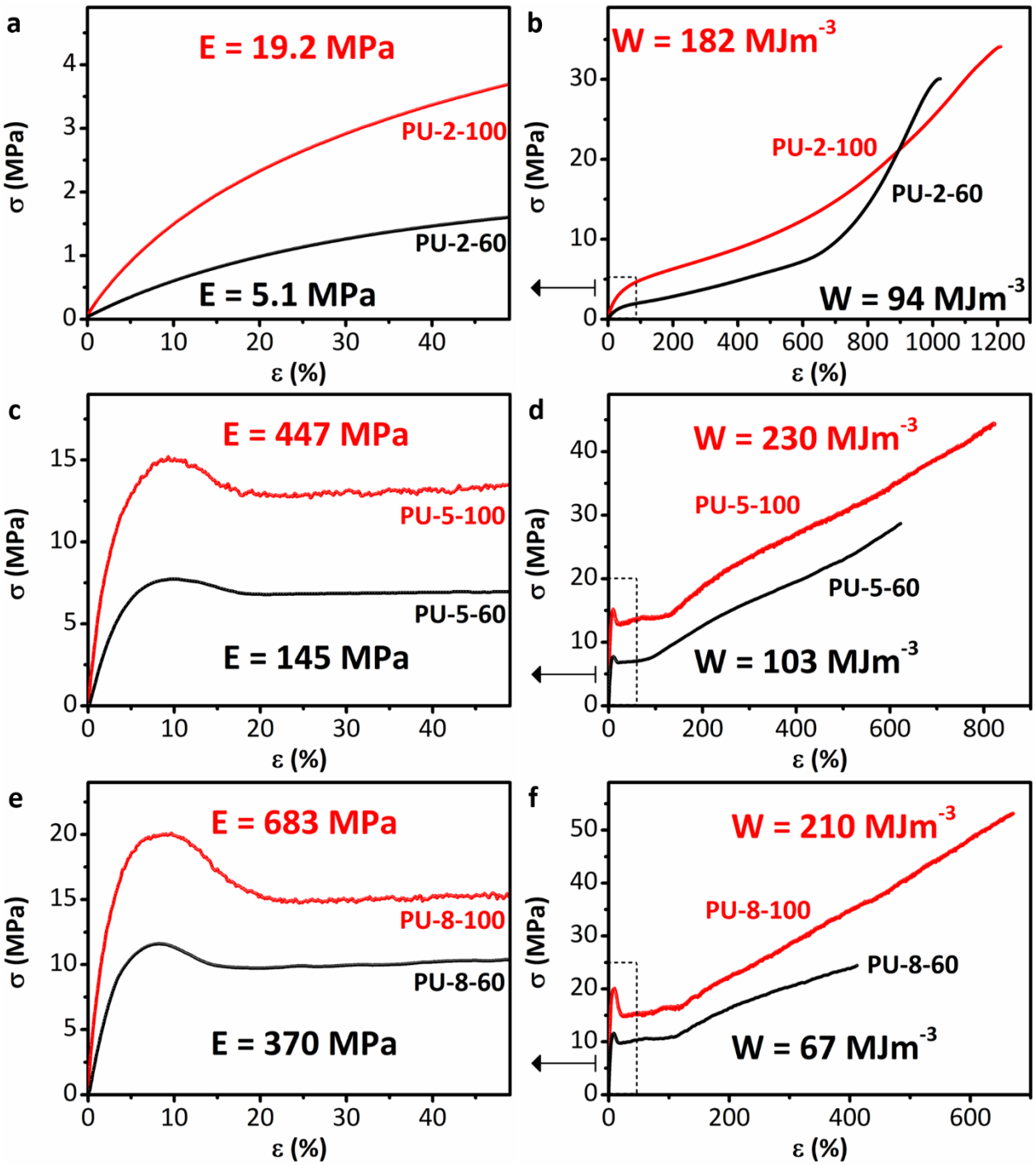

Figure 24. Expanded initial regions and complete stress-strain curves of the PU copolymers under investigation: (a-b) PU-2-60 vs. PU-2-100, (c-d) PU-5-60 vs. PU-5-100, (e-f) PU-8-60 vs. PU-8-100. E: Elastic modulus, W: Toughness (work to fracture).

These enhancements arisen from the change in drying temperature are mainly attributed to the structural and morphological changes along the multiple length scales demonstrated in previous sections. More specifically, the hierarchical self-assembly of tightly-packed secondary structures along the multiple length scales based on the confined crystallization of PEO chains in subnanometer urea channels in the samples dried at 100 °C is the main reason for notable increases in their mechanical properties as compared to those of the samples dried at 60 °C since this enables the structural elements involved

in this hierarchical architecture to work cooperatively and maintain a homogeneous deformation state at each hierarchical level along the multiple length scales. This is because the formation of α–complex crystals ensures the confinement of key secondary structures and hence, the hydrogen bonds. When confined, hydrogen bonds are deformed within a small region corresponding to the size of several bonds in which the deformation and rupture of hydrogen bonds are delocalized. The formation of α–complex crystals means a greatly increased density of hydrogen bonds and the formation of densely packed interlocking regions where hydrogen bonds act in "confined" state (delocalized deformation) that ensures an effective load transfer between the chains under tension. Densely packed hydrogen bonds in these crystalline regions eventually break and allow strands of secondary structures to slide, leading to the separation of smaller intact crystals. This markedly contributes to the strength, extensibility and toughness.

Table 3. Mechanical properties of the PU films investigated.

Sample	E (MPa)	σ_y (MPa)	σ_{max} (MPa)	ε (%)	W (MJm^{-3})
PU-2-60	5.1±0.3	-	30.1±1.1	1000±64	94.0±6.7
PU-2-100	19.2±2.8	-	34.2±1.6	1240±48	182±9.3
PU-5-60	145±19	7.72±0.8	28.7±1.3	627±51	103±7.8
PU-5-100	447±23	15.7±1.1	44.9±2.4	823±42	230±14
PU-8-60	370±20	11.6±0.7	24.4±3.4	412±33	67.2±5.7
PU-8-100	683±36	20.0±0.4	53.2±5.1	675±27	210±12

For PU-2, the geometric confinement is limited to the confinement of hydrogen bonds in α–complex crystals. Hence, from a mechanical point of view, the presence of α–complex crystals solely suggests a more robust elastomeric network for PU-2 based samples. The E, σ_{max}, ε, W of PU-2-100 are therefore higher than those of PU-2-60. However, the formation of α–complex crystals is even more important for PU-5 and PU-8 since it leads up to the geometric confinement of other structural elements, such as soft segment crystals (7_2-helix), changes the entire structural hierarchy along the multiple length scales, and hence, influences each deformation regime under tension. In this case, the geometric confinement is not only limited to the confinement of hydrogen bonds in α–complex crystals. These nanocrystals, and hence 4_1-helices and β–sheets, along with helical soft segment crystals are also confined into the compact globular domains (Figure 23). At nanoscale, these compact globular domains (Figure 23) can be considered as the three-dimensional "composite" network of different secondary structures that stiff complex nanocrystals containing 4_1-helices and β–sheets embedded in a semi-crystalline matrix with 7_2-helices. Under tension, this three-dimensional "composite" network shows a distinct elastic response up to a yield point. At the yield, hydrogen bonds in relatively more disordered secondary structures in the matrix phase break and hence the materials undergoes a softening regime in which the semi-crystalline matrix phase unfolds along

the stretching direction. The softening is mainly due to the unravelling of hidden length unlocked as a result of the rupture of hydrogen bonds. This is then followed by a stiffening regime where the load is mainly transferred from fully-extended matrix phase to stiff complex nanocrystals whose plastic deformation eventually resulting in failure.

At microscale, the geometric confinement along the multiple length scales leads to a microstructure that consists of homogeneously distributed small microcrystals and does not have sharp grain boundries. This means that these microcrystals are also in a confined state. This explains why PU-5-100 and PU-8-100 have greater stiffness and strength compared to PU-5-60 and PU-8-60 which have a lot bigger microcrystals and sharp grain boundries. Hence, the geometric confinement along the multiple length scales plays a key role in achieving remarkably enhanced stiffness, strength, extensibility and toughness.

4. CONCLUSION

Here we mainly conclude that geometric confinement governs stiffness, strength, extensibility and toughness in sol-cast PU films. Soft segment molecular weight and drying temperature are demonstrated to be practical and effective design/processing parameters to tune the severity of geometric confinement. This approach, i.e., tuning the severity of geometric confinement via simple parameters, can be utilized to produce advanced PU based materials with well-defined hierarchical structures and desired functional properties, and hence, to address the challenge of attaining unprecedented combinations of stiffness, strength, extensibility and toughness.

In line with this main conclusion, several important findings may be highlighted as follow:

- Governing mechanism behind the structure formation in the PU copolymers investigated displays significant variations depending on soft segment molecular weight and drying conditions. On one hand, phase mixing plays a key role for final morphology and associated properties of the PU-2 copolymer, when its sol-cast films are dried at 60 °C as demonstrated in PU-2-60. No notable confinement is observed for this sample. On the other hand, the structure formation is mainly driven by the confined crystallization of PEO chains in subnanometer urea channels, which gives rise to the formation of α-complex crystals, and the final morphology consists of “micro-phase separated” clusters of these complex crystals at larger length scales, when they are dried at 100 °C as shown in PU-2-100. The geometric confinement is only limited to the primary and secondary structures forming the α-complex crystals. No confinement is observed at larger length scales.
- For PU-5 and PU-8, bulk crystallization of the PEO soft segments controls the structure formation and hence the final semi-crystalline (spherulitic) morphology governs their structure-property relations, when their sol-cast films are dried at 60 °C as demonstrated in PU-5-60 and PU-8-60. The geometric confinement in these samples

is only limited to the conformation of ethylene oxide units in the PEO crystals. There is no considerable confinement at larger length scales, especially at micro-level. When they are dried at 100 °C, an elegant hierarchical self-assembly (spanning length scales from angstroms to micrometers) is observed as shown in PU-5-100 and PU-8-100. The geometric confinement is of particular importance for this structural hierarchy responsible for a unique combination of mutually exclusive mechanical properties, i.e. stiffness, strength, extensibility and toughness. The structure formation in these samples is driven by the confined crystallization of helical PEO chains in subnanometer urea channels and complemented by the "bulk" crystallization of PEO matrix phase and/or the micro-phase separation. In this case, the "bulk" crystallization of PEO matrix phase also takes place in a confined space as due to the presence of α-complex crystals. However, we use the term "bulk" here to distinguish these two crystallization mechanisms from each other. In addition, the micro-phase separation here refers to the "separation" of the crystalline domains from the amorphous regions at larger length scales. Overall, these samples show severe geometric confinement.

- The structural hierarchy demonstrated here contains synthetic replica of natural design motifs like helices, anti-parallel β-sheets, β-turns with dimensional features comparable to those found in native structures. Hence, our findings might be of interest in mimicking certain protein structures containing these design motifs.
- In addition to the structural changes highlighted above, it should be noted that the increase in total crystallinity is also important for a better understanding of the significant variations in mechanical properties.

ASSOCIATED CONTENT

Supporting Information

The Supporting Information is available free of charge on the ACS Publications website (http://pubs.acs.org/). Figure S1 shows DSC thermograms of the hard segment model compounds. Their XRD patterns are also shown in Figure S2. Figure S3 displays chemical structure of the PU copolymers investigated. Figure S4 shows their TGA curves. Figure S5 and S6 display the deconvoluted peaks in the amide-I regions of the ATR-IR spectra of PU-2-100 and PU-5-100, respectively. Figure S7-S9 show the deconvoluted amide-II peaks for PU-2-100, PU-5-100 and PU-8-100, respectively. Amide-II peak of the 4_1-helix is observed at 1550 cm^{-1} for PU-2-100, whereas it is found at 1557 cm^{-1} for both PU-5-100 and PU-8-100. Amide-II peaks of the β-sheet are also detected at 1535 cm^{-1} and 1515 cm^{-1} for these two samples. The respective peaks are apparent at 1535 cm^{-1} and 1516 cm^{-1} for PU-2-100. In addition, Figure S10 shows AFM phase images of PU-2-60 with scale bars of 2 μm (Figure S10a) and 50 nm (Figure 10b) representing the morphology along the multiple length scales.

Finally, Figure S11 displays OM images of PU-8-60 (Figure S11a) and PU-8-100 (Figure S11b) recorded at 60 °C, which is well above the melting point of PEO crystals in the samples.

AUTHOR INFORMATION

Corresponding authors

Oguzhan Oguz – *Faculty of Engineering and Natural Sciences, Materials Science and Nano Engineering, Sabanci University, 34956, Orhanli, Tuzla, Istanbul, Turkey; Sabanci University Integrated Manufacturing Technologies Research and Application Center & Composite Technologies Center of Excellence, Teknopark Istanbul, 34906 Pendik, Istanbul, Turkey; ORCID: 0000-0002-4457-5274; E-mail: oguzhanoguz@sabanciuniv.edu*

Iskender Yilgor – *KUYTAM Surface Science and Technology Center, Chemistry Department, Koc University, 34450, Sariyer, Istanbul, Turkey*; *E-mail: iyilgor@ku.edu.tr*

Yusuf Z. Menceloglu – *Faculty of Engineering and Natural Sciences, Materials Science and Nano Engineering, Sabanci University, 34956, Orhanli, Tuzla, Istanbul, Turkey; Sabanci University Integrated Manufacturing Technologies Research and Application Center & Composite Technologies Center of Excellence, Teknopark Istanbul, 34906 Pendik, Istanbul, Turkey; ORCID: 0000-0003-0296-827X; E-mail: yusufm@sabanciuniv.edu*

Authors

Nicolas Candau – *Centre Català del Plàstic (CCP) - Universitat Politècnica de Catalunya Barcelona Tech (EEBE-UPC), Av. D'Eduard Maristany, 16, 08019, Spain*

Grégory Stoclet – *Unité Matériaux Et Transformations (UMET), UMR CNRS 8207, Université de Lille Nord de France, USTL-ENSCL, Bat C7, BP 90108, 59652 Villeneuve d'Ascq, France*

Eren Simsek – *Faculty of Engineering and Natural Sciences, Materials Science and Nano Engineering, Sabanci University, 34956, Orhanli, Tuzla, Istanbul, Turkey; Current Address: Quantag Nanotechnologies, Barbaros, 34746, Istanbul, Turkey*

Cagla Kosak Soz – *KUYTAM Surface Science and Technology Center, Chemistry Department, Koc University, 34450, Sariyer, Istanbul, Turkey*

Emel Yilgor – *KUYTAM Surface Science and Technology Center, Chemistry Department, Koc University, 34450, Sariyer, Istanbul, Turkey*

Notes

The authors declare no competing financial interest.

ACKNOWLEDGEMENTS

We acknowledge Scientific and Technical Research Council of Turkey (TUBITAK) for the use of materials which were synthesized within the scope of the project funded under the contact number of 109M073.

REFERENCES

(1) Noshay, A.; McGrath, J. E. *Block Copolymers: Overview and Critical Survey*. Elsevier Science: **2013**.

(2) Szycher, M. *Szycher's Handbook of Polyurethanes, First Edition*. Taylor & Francis: **1999**.

(3) C. Prisacariu, C. *Polyurethane Elastomers: From Morphology to Mechanical Aspects*. Springer, Verlag/Wien, **2011**.

(4) Yilgor, I; Yilgor, E; Wilkes, G. L. Critical parameters in designing segmented polyurethanes and their effect on morphology and properties: A comprehensive review. *Polymer* **2015,** *58,* A1–A36.

(5) Yilgor, I; Yilgor, E. Structure-Morphology-Property Behavior of Segmented Thermoplastic Polyurethanes and Polyureas Prepared without Chain Extenders, *Polym. Rev*. **2007,** *47,* 487–510.

(6) Delebecq, E.; Pascault, J. P.; Boutevin, B.; Ganachaud, F. On the Versatility of Urethane/Urea Bonds: Reversibility, Blocked Isocyanate, and Non-isocyanate. *Chem. Rev.* **2013,** *113,* 80−118.

(7) Krol, P. Synthesis methods, chemical structures and phase structures of linear polyurethanes. Properties and applications of linear polyurethanes in polyurethane elastomers, copolymers and ionomers. *Prog. Mater. Sci.* **2007**, *52,* 915–1015.

(8) Seven-Avaz, S.; Oguz, O.; Menceloglu, Y. Z.; Atilgan, C. Tuning Interaction Parameters of Thermoplastic Polyurethanes in a Binary Solvent To Achieve Precise Control over Microphase Separation. *J. Chem. Inf. Model.* **2019**, *59*, 1946–1956.

(9) Choi, T.; Weksler, J.; Padsalgikar, A.; Runt, J. Influence of soft segment composition on phase-separated microstructure of polydimethylsiloxane-based segmented polyurethane copolymers. *Polymer* **2009**, *50*, 2320–2327.

(10) Lu, Y.; Larock, R. C. 2008. Soybean-oil-based waterborne polyurethane dispersions: effects of polyol functionality and hard segment content on properties. *Biomacromolecules* **2008**, *9*, 3332–3340.

(11) Chattopadhyay, D. K.; Sreedhar, B.; Raju, K. V. 2005. Effect of chain extender on phase mixing and coating properties of polyurethane ureas. *Ind. Eng. Chem. Res.* **2005**, *44*, 1772–1779.

(12) Hojabri, L.; Kong, X.; Narine, S. S. Fatty acid-derived diisocyanate and biobased polyurethane produced from vegetable oil: synthesis, polymerization, and characterization. *Biomacromolecules* **2009**, *10*, 884–891.

(13) Kojio, K.; Nozaki, S.; Takahara, A.; Yamasaki, S. 2020. Influence of chemical structure of hard segments on physical properties of polyurethane elastomers: a review. *J. Polym. Res.* **2020**, 27, 1–13.

(14) Wilkes, G. L.; Wildnauer, R. Kinetic behavior of the thermal and mechanical properties of segmented urethanes. *J. Appl Phys.* **1975,** *46,* 4148–4152.

(15) Wilkes, G. L.; Emerson, J. A. Time dependence of small-angle x-ray measurements on segmented polyurethanes following thermal treatment. *J. Appl Phys.* **1976,** 47, 4261–4264.

(16) Wilkes, G. L.; Dziemianowicz, T. S.; Ophir, Z. H.; Artz, E.; Wildnauer, R. Thermally induced time dependence of mechanical properties in biomedical grade polyurethanes. *J. Biomed. Mater. Res. A.* **1979,** *13,* 189–206.

(17) Hesketh, T. R.; Van Bogart, J. W. C.; Cooper, S. L. Differential scanning calorimetry analysis of morphological changes in segmented elastomers. *Polym. Eng. Sci.* **1980,** *20,* 190–197.

(18) Van Bogart, J. W. C.; Bluemke, D. A.; Cooper, S. L. Annealing-induced morphological changes in segmented elastomers. Polymer **1981,** *22,* 1428–1438.

(19) Hu, W.; Koberstein, J. T. The effect of thermal annealing on the thermal properties and molecular weight of a segmented polyurethane copolymer. *J. Polym. Sci. Part B Polym. Phys.* **1994,** *32,* 437–446.

(20) Phillips, R. A.; Cooper, S. L. Morphology development during solid-state annealing of poly (ether-ester) multiblock copolymers. *J. Polym. Sci. Part B Polym. Phys*. **1996,** *34,* 737–749.

(21) Yanagihara, Y.; Osaka, N.; Murayama, S.; Saito, H. Thermal annealing behavior and structure development of crystalline hard segment domain in a melt-quenched thermoplastic polyurethane. *Polymer* **2013,** *54,* 2183–2189.

(22) Yanagihara, Y.; Osaka, N.; Iimori, S.; Murayama, S.; Saito, H. Relationship between modulus and structure of annealed thermoplastic polyurethane. *Mater. Today Commun.* **2015,** *2,* e9–e15.

(23) Oguz, O.; Simsek, E.; Kosak Soz, C.; Kasli Heinz, O.; Yilgor, E.; Yilgor, I.; Menceloglu, Y. Z. Effect of filler content on the structure-property behavior of poly(ethylene oxide) based polyurethaneurea-silica nanocomposites. *Polym. Eng. Sci.* **2018,** *58***,** 1097–1107.

(24) Korley, L. S. T. J.; Pate, B. D.; Thomas E. L.; Hammond, P. T. Effect of the degree of soft and hard segment ordering on the morphology and mechanical behavior of semicrystalline segmented polyurethanes. *Polymer* **2006**, *47,* 3073–3082.

(25) Huang, Y.C.; Huang, Y.H.; Chen, L.Y.; Dai, C.A.; Dai, S.A.; Chen, Y.H.; Wu, C.H.; Jeng, R.J. 2021. Robust thermoplastic polyurethane elastomers prepared from recycling polycarbonate. *Polymer*, **2021**, *212*, No. 123296.

(26) Bailey, F. E.; Koleske, J. V. *Poly(ethylene oxide)*. Academic Press, **1976**.

(27) Harris, J. M. ed. *Poly (ethylene glycol) chemistry: biotechnical and biomedical applications.* Springer Science & Business Media: **2013**.

(28) Oguz, O. Koutsoumpis, S. A.; Simsek, E.; Yilgor, E.; Yilgor, I.; Pissis, P.; Menceloglu, Y. Z. Effect of soft segment molecular weight on the glass transition, crystallinity, molecular mobility and segmental dynamics of poly (ethylene oxide) based poly (urethane–urea) copolymers. *RSC Adv.* **2017,** *7*, 40745–40754.

(29) Koutsoumpis, S.; Raftopoulos, K. N.; Oguz, O.; Papadakis, C.; Menceloglu, Y. Z.; Pissis, P. Dynamic Glass Transition of the Rigid Amorphous Fraction in Polyurethane-urea/SiO_2 Nanocomposites. *Soft Matter* **2017**, *13*, 4580–4590.

(30) Avaz, S.; Oguz, O.; Kurt, H.; Menceloglu, Y. Z.; Atilgan, C. Soft segment length controls morphology of poly (ethylene oxide) based segmented poly (urethane-urea) copolymers in a binary solvent. *Comput. Mater. Sci.* **2017**, *138*, 58–69.

(31) Malay, O.; Oguz, O.; Kosak, C.; Yilgor, E.; Yilgor, I.; Menceloglu, Y. Z. Polyurethaneurea–silica nanocomposites: preparation and investigation of the structure–property behavior. *Polymer* **2013**, *54*, 5310–5320.

(32) Oguz, O.; Candau, N.; Bernhard, S. H.; Kosak Soz, C.; Heinz, O.; Stochlet, G.; Plummer, C. J.; Yilgor, E.; Yilgor, I.; Menceloglu, Y. Z. Effect of surface modification of colloidal silica nanoparticles on the rigid amorphous fraction and mechanical properties of amorphous polyurethane–urea–silica nanocomposites. *J. Polym. Sci. Part A Polym. Chem.* **2019**, *57*, 2543–2556.

(33) Qiu, W.; Pyda, M.; Nowak-Pyda E.; Habenschuss, A.; Wunderlich, B. Reversibility between glass and melting transitions of poly(oxyethylene). *Macromolecules* **2005,** *38,* 8454–8464.

(34) Raftopoulos, K. N.; Koutsoumpis, S.; Jancia, M.; Lewicki, J. P.; Kyriakos, K.; Mason, H. E.; Harley, S. J.; Hebda, E.; Papadakis, C. M.; Pielichowski, K.; Pissis, P. Reduced Phase Separation and Slowing of Dynamics in Polyurethanes with Three-Dimensional POSS-Based Cross-Linking Moieties. *Macromolecules* **2015,** *48,* 1429−1441.

(35) Wunderlich, B. *Thermal Analysis of Polymeric Materials*, Springer, Berlin Heidelberg, **2005**.

(36) Saiani, A.; Daunch, W. A.; Verbeke, H.; Leenslag, J. W.; Higgins, J. S. Origin of multiple melting endotherms in a high hard block content polyurethane. 1. Thermodynamic investigation. *Macromolecules* **2001,** *34,* 9059–9068.

(37) Poręba, R.; Špírková, M.; Brožová, L.; Lazić, N.; Pavličević, J.; Strachota, A. Aliphatic polycarbonate-based polyurethane elastomers and nanocomposites. II. Mechanical, thermal, and gas transport properties. *J. Appl. Polym. Sci.* **2013**, *127*, 329–341.

(38) Koberstein, J. T.; Russell, T. P. Simultaneous SAXS-DSC study of multiple endothermic behavior in polyether-based polyurethane block copolymers, *Macromolecules* **1986**, *19,* 714–720.

(39) Yoshihara, T.; Tadokoro, H.; Murahashi, S.; Normal Vibrations of the Polymer Molecules of Helical Conformation. IV. Polyethylene Oxide and Polyethylene$_4$ Oxide. *J. Chem. Phys.* **1964,** *41,* 2902.

(40) French, A. C.; Thompson, L. A.; Davis, B. G. High-Purity Discrete PEG-Oligomer Crystals Allow Structural Insight. *Angew. Chem. Int. Ed.* **2009,** *48,* 1248–1252.

(41) Chrissopoulou, K.; Andrikopoulos, K. S.; Fotiadou, S.; Bollas, S.; Karageorgaki, C.; Christofilos, D.; Voyiatzis, G. A.; Anastasiadis, S. H. Crystallinity and chain conformation in PEO/layered silicate nanocomposites. *Macromolecules* **2011,** *44,* 9710–9722.

(42) Kwon, O. H.; Ortalan, V.; Zewail, A. H. Macromolecular structural dynamics visualized by pulsed dose control in 4D electron microscopy. *Proc. Natl Acad. Sci. USA* **2011,** *108,* 6026–6031.

(43) Kim, S. A.; Archer, L. A. Hierarchical Structure in Semicrystalline Polymers Tethered to Nanospheres. *Macromolecules* **2014,** *47,* 687–694.

(44) Powder Diffraction File Card No: 00–008–0822, JCPDS–International Centre for Diffraction Data, Newtown Square PA, **2016**.

(45) Chenite, A.; Brisse, F. Structure and Conformation of Poly(ethylene oxide), PEO, in the Trigonal Form of the PEO-Urea Complex at 173 K, *Macromolecules* **1991,** *24,* 2221-2225.

(46) Vasanthan, N.; Shin, I. D.; Tonelli, A. E. Structure, conformation, and motions of poly (ethylene oxide) and poly (ethylene glycol) in their urea inclusion compounds. *Macromolecules* **1996**, *29,* 263–267.

(47) Liu, Y.; Pellerin, C. Highly Oriented Electrospun Fibers of Self-Assembled Inclusion Complexes of Poly(ethylene oxide) and Urea. *Macromolecules* **2006,** *39,* 8886-8888.

(48) Ye, H. M.; Peng, M.; Xu, J.; Guo, B. H.; Chen, Q.; Yun, T. L.; Ma, H. Conformation transition and molecular mobility of isolated poly(ethylene oxide) chains confined in urea nanochannels. *Polymer* **2007,** *48,* 7364-7373.

(49) Liu, Y.; Antaya, H.; Pellerin, C. Characterization of the Stable and Metastable Poly(ethylene oxide)–Urea Complexes in Electrospun Fibers. *J. Polym. Sci. Part B Polym. Phys*. **2008,** *46,* 1903–1913.

(50) Liu, Y.; Pellerin, C. Stability and phase behavior of the poly(ethylene oxide)–urea complexes prepared by electrospinning. *Polymer* **2009,** *50,* 2601–2607.

(51) Ye, H. M.; Song, Y. Y.; Xu, J.; Guo, B. H.; Zhou, Q. Melting behavior of inclusion complex formed between polyethylene glycol oligomer and urea. *Polymer* **2013**, *54,* 3385-3391.

(52) Thakral, S. Study of moisture sorption behavior of urea inclusion compounds with aliphatic guests and with linear polymers. *J. Phys. Org. Chem.* **2014,** *27,* 76–86.

(53) Homminga, D.; Goderis, B.; Dolbnya, I.; Reynaers, H.; Groeninckx, G. Crystallization behavior of polymer/montmorillonite nanocomposites. Part I. Intercalated poly(ethylene oxide)/montmorillonite nanocomposites. *Polymer* **2005,** *46,* 11359–11365.

(54) Schönherr, H.; Frank, C. W. Ultrathin films of poly (ethylene oxides) on oxidized silicon. 1. Spectroscopic characterization of film structure and crystallization kinetics, *Macromolecules* **2003,** *36,* 1188–1198.

(55) Koenig J. L.; Angood, A. C. Raman spectra of poly (ethylene glycols) in solution, *J. Polym. Sci. Part B Polym. Phys*. **1970**, *8,* 1787–1796.

(56) Maxfield J.; Shepherd, I. W. Conformation of poly(ethylene oxide) in the solid state, melt and solution measured by Raman scattering, *Polymer* **1975**, *16,* 505–509.

(57) Matsuura, H.; Fukuhara, K. Vibrational spectroscopic studies of conformation of poly(oxyethylene). II. Conformation–spectrum correlations, *J. Polym. Sci. Part B Polym. Phys*. **1986,** *24,* 1383–1400.

(58) Vollrath, F.; Knight, D. P. 2001. Liquid crystalline spinning of spider silk. *Nature* **2001,** *410*, 541.

(59) Porter, D.; Vollrath, F. Silk as a biomimetic ideal for structural polymers. *Adv. Mater.* **2009**, *21*, 487–492.

(60) Holland, C.; Vollrath, F.; Ryan, A. J.; Mykhaylyk, O. O. Silk and synthetic polymers: reconciling 100 degrees of separation. Adv. Mater. **2012,** *24*, 105–109.

(61) Buehler, M. J. 2010. Tu (r) ning weakness to strength. *Nano Today* **2010,** *5*, 379–383.

(62) Keten, S.; Xu, Z.; Ihle, B.; Buehler, M. J. Nanoconfinement controls stiffness, strength and mechanical toughness of β-sheet crystals in silk. *Nat. Mater.* **2010,** *9*, 359.

(63) Tarakanova, A.; Buehler, M. J. A materiomics approach to spider silk: protein molecules to webs. *Jom* **2012**, *64*, 214–225.

(64) Kluge, J. A.; Rabotyagova, O.; Leisk, G. G.; Kaplan, D. L. 2008. Spider silks and their applications. *Trends Biotechnol.* **2008,** *26*, 244–251.

(65) Omenetto, F. G.; Kaplan, D. L. New opportunities for an ancient material. *Science* **2010,** *329*, 528–531.

(66) Tokareva, O.; Jacobsen, M.; Buehler, M.; Wong, J.; Kaplan, D. L. Structure–function–property–design interplay in biopolymers: Spider silk. *Acta Biomater.* **2014,** 10, 1612–1626.

(67) Johnson, J. C.; Wanasekara, N. D.; Korley, L. S. T. J. 2014. Influence of secondary structure and hydrogen-bonding arrangement on the mechanical properties of peptidic-polyurea hybrids. *J. Mater. Chem. B* **2014,** 2, 2554–2561.

(68) Tanaka, S.; Ogura, A.; Kaneko, T.; Murata, Y.; Akashi, M. Precise synthesis of ABA triblock copolymers comprised of poly (ethylene oxide) and poly (β-benzyl-l-aspartate): a hierarchical structure inducing excellent elasticity. *Macromolecules* **2004,** *37*, 1370–1377.

(69) Rathore, O.; Sogah, D. Y. 2001. Self-assembly of β-sheets into nanostructures by poly (alanine) segments incorporated in multiblock copolymers inspired by spider silk. *J. Am. Chem. Soc.* **2001,** *123*, 5231–5239.

(70) Rathore, O.; Sogah, D. Y. Nanostructure formation through β-sheet self-assembly in silk-based materials. *Macromolecules* **2001,** *34,* 1477–1486.

(71) Yilgor, I.; Yilgor, E.; Guler, I. G.; Ward, T. C.; Wilkes, G. L. FTIR investigation of the influence of diisocyanate symmetry on the morphology development in model segmented polyurethanes. *Polymer* **2006,** *47*, 4105–4114.

(72) Rabotyagova, O. S.; Cebe, P.; Kaplan, D. L. Role of Polyalanine Domains in β-Sheet Formation in Spider Silk Block Copolymers. *Macromol. Biosci.* **2010,** *10*, 49–59.

(73) Versteegen, R. M.; Kleppinger, R.; Sijbesma, R. P.; Meijer, E. W. Properties and Morphology of Segmented Copoly(ether urea)s with Uniform Hard Segments. *Macromolecules* **2006,** *39,* 772–783.

(74) Kautz, H.; van Beek, D. J. M.; Sijbesma, R. P.; Meijer, E. W. Cooperative End-to-End and Lateral Hydrogen-Bonding Motifs in Supramolecular Thermoplastic Elastomers *Macromolecules,* **2006,** *39,* 13.

(75) Koevoets, R. A.; Versteegen, R. M.; Kooijman, H.; Spek, A. L.; Sijbesma, R. P.; Meijer, E. W. Molecular Recognition in a Thermoplastic Elastomer**,** *J. Am. Chem. Soc.* **2005,** *127,* 2999–3003.

(76) Chan, H. S.; Dill, K. A. Origins of structure in globular proteins. *Proc. Natl Acad. Sci. USA* **1990**, *87*, 6388–6392.